Water availability and atmospheric dryness controls on spaceborne sun-induced chlorophyll fluorescence yield

S. De Cannière[a,*], M.J. Baur[b], D. Chaparro[c], T. Jagdhuber[c,d], F. Jonard[e,f]

[a]*Earth and Life Institute, Université catholique de Louvain, Croix du Sud 2 Box L7.05.02, 1348 Louvain-la-Neuve, Belgium*
[b]*Department of Geography, University of Cambridge, CB2 3EN Cambridge, UK*
[c]*Microwaves and Radar Institute, German Aerospace Center (DLR), 82234, Wessling, Germany*
[d]*Faculty of applied computer science: Institute of Geography, Universität Augsburg, 86159 Augsburg, Germany*
[e]*Earth Observation and Ecosystem Modelling Laboratory, SPHERES Research unit, Universté de Liège, 4000 Liège, Belgium*
[f]*Agrosphere (IBG-3), Institute of Bio- and Geosciences, Forschungszentrum Jülich GmbH, 52425 Jülich, Germany*

Abstract

Climate change is amplifying the duration, frequency, and intensity of droughts, harming global ecosystems. During droughts, plants can close their stomata to save water, at the expense of a reduced carboxylation rate. When in a carboxylation-limited regime, plants benefit from an increase in water availability, as it increases their photosynthetic rate. The sun-induced chlorophyll fluorescence (SIF) signal, measurable from satellites, is mechanistically linked to this rate. Like canopy photosynthesis, SIF carries an imprint from the available irradiation (PAR) as well as on the canopy structure and on the efficiency of the photosynthesis at the photosystem level. Normalizing the global TROPOMI SIF observations with TROPOMI reflectance and MODIS Normalised Difference Vegetation Index (NDVI) data, we extracted the fluorescence quantum yield (ϕ_F), which lab-scale experiments have found to

---

[*] Corresponding author

be linked to the photosynthetic electron transport. Plant physiologists have long proved the photosynthetic electron transport to be sensitive to plant water status conditions. Here, the plant water status is controlled by the soil moisture (SM) and the vapour pressure deficit (VPD). Combining data from the TROPOMI, AIRS and SMAP satellite sensors, this study describes how SM and VPD control the ϕ_F at the global scale. We identify a VPD range (VPD<1.5 kPa) in which the ϕ_F is mainly controlled by VPD, and another (VPD>1.5 kPa) in which the ϕ_F is co-regulated by SM and VPD. The precise values of this range, as well as the magnitude of ϕ_F values are modulated by the plant isohydricity. To gain a deeper understanding of the link between ϕ_F and photosynthetic efficiency at large scale, we used the link between ϕ_F and data on the canopy conductance (Gs), which were calculated using remote sensing data-driven models. A comparison found that the ϕ_F-Gs relationship at large scale is in line with the ϕ_F-Gs relationship described in plant-level studies.

1. Introduction

Water is an essential element for plants to grow and for ecosystems to function. Changes in the ecosystem water status jeopardize the ecosystem health, reduce crop yields and may lead to forest fires, among other impacts (Gupta et al., 2020; O et al., 2020; Venturas et al., 2021). Due to climate change, droughts are an increasingly relevant problem in the coming decades (Balting et al., 2021). From a plant physiological perspective, a drought is a shortage of water availability, combined with high atmospheric water demand (Orimoloye, 2022). This induces a series of possible reactions, which include stomatal closure, decreased photosynthetic rate, leaf water loss, cavitation, chlorophyll degradation and accelerated senescence (West et al., 2019; Jonard et al., 2011). Over the last 50 years, remote sensing has proven its value for large-scale drought stress monitoring. First-generation Earth Observation (EO) satellites have used the canopy greenness as an indicator of an ecosystem's stress status (West et al., 2018), as damaged plants tend to shed or brown their leaves. While very intuitive, greenness only provides limited information on plant physiology. Data streams generated by new-generation EO satellites are focused on signals that are more closely linked to plant health, establishing a link between the fields of plant physiology and remote sensing (Jonard et al., 2020). A key variable in this school of thought is the sun-induced chlorophyll fluorescence (SIF) signal, which originates in the heart of the photosynthetic apparatus (Porcar-Castell et al., 2021).

Photosynthesis is the process by which a plant harvests light energy and uses it to incorporate a CO_2 molecule into a carbohydrate. This overall reaction can be split into two main processes: the photosynthetic electron transport, responsible for the light harvesting, and the Calvin cycle, responsible for the CO_2 assimilation (Farquhar et al., 1980). The chlorophyll molecules are embedded in proteins forming photosystems (PS). The activity of photosystem II (PSII) determines the rate of light absorption, while the rate of the Calvin cycle is determined by the carboxylation rate. On the one hand, the overall photosynthetic rate is limited by its light reactions, thus by its energy availability. On the other hand, water availability conditions control the carboxylation regime, as plants tend to close their stomata reducing transpiration in an attempt to save water at the expense of a reduced CO_2 uptake

(Muhammad et al., 2021; Jonard et al., 2022).

The mechanistic link between SIF and photosynthesis finds its origins at the level of PSII. The PSII is responsible for the electron harvesting from a water molecule and for sending it to the electron transport chain. For a PSII to provide this energy, its outermost electron pair jumps to a higher energy level, forming an excited PSII (PSII*). The energy trapped by this photosystem is split over three pathways. The first pathway is the photochemical electron chain, fuelling the Calvin cycle. The second pathway is a container category of processes that dissipate the excess trapped energy as heat. These are collectively known as non-photochemical quenching (NPQ). As a final pathway, the trapped photon can be re-emitted as chlorophyll fluorescence (Porcar-Castell et al., 2014). The fraction of photons going down each pathway is referred to as the photochemical quantum yield (ϕ_p), the non-photochemical quantum yield (ϕ_N), and the fluorescence quantum yield (ϕ_F), respectively. The ϕ_F emission typically varies between 1 and 3% of the absorbed light radiation (Jonard et al., 2020). A lowered carboxylation decreases the energy demand by the photosynthetic electron transport chain, decreasing ϕ_P, increasing ϕ_N, which leads to a decrease in the life-time of the excited state of photosystem II (PSII*), decreasing ϕ_F (van der Tol et al., 2014). Consequently, it was possible to link ϕ_F to stomatal conductance (Gs) using leaf-level measurements (Flexas et al., 2002). Canopy-scale SIF is the aggregate of the fluorescence emission of all photosystems, the rate of which is determined by ϕ_F. Therefore, ϕ_F can be conceptualized as the physiological component of SIF.

SIF is dwarfed by the reflected and scattered sunlight, restricting the

SIF retrieval to the Fraunhofer lines and Telluric bands. These are (sub-)nanometre scale spectral bands in which solar irradiation is reduced. In case of the Fraunhofer lines, this reduction is caused by light absorption by -mostly metallic- elements in the Sun's outer layers. In Telluric lines, the reduction is caused by atmospheric gasses. The main Telluric lines are linked to absorption of O_2 and of H_2O. Thanks to the reduction in solar irradiation in the Fraunhofer lines, the relative contribution of SIF to the measured radiance is significantly higher compared to radiances measured outside these bands. Given the narrow spectral range of the Fraunhofer lines, a nanometre-scale spectral resolution is imperative for SIF measurements. The FLuorescence EXplorer (FLEX) satellite, scheduled for launch in 2025, will be carrying two terrspectrometers tailored to SIF retrievals (Drusch et al., 2017). Currently, satellites designed for monitoring atmospheric trace gasses provide global SIF data products. One of these products comes from the TROPOspheric Monitoring Instrument (TROPOMI), installed on Sentinel-5P, that provides daily global coverage. Guanter et al. (2021) propose two different TROPOMI-based SIF products that estimate the SIF emission at 740 nm. The product differ in the fitting window through which SIF is retrieved; the 735 product makes use of a fitting window between 735 and 758 nm, while the 743 product uses a fitting window between 743 and 758 nm. The former makes use of a wider range of Fraunhofer lines than the latter, but its retrieval is impacted by the atmospheric water content. The latter only uses solar absorption lines, making the retrievals independent from the atmospheric water content.

Given its use in the field of plant physiology, there is an increasing interest in finding remote sensing based estimates of ϕ_F. Tower- or drone-based remote sensing studies have retrieved ϕ_F at the canopy scale and managed to observe a reaction in ϕ_F in function of the water availability (De Cannière et al., 2021; De Canniere et al., 2022; Wang et al., 2023; Xu et al., 2021). Similarly, Kimm et al. (2021a) pointed out the importance of the water demand, quantified by the vapour pressure deficit (VPD). Both high VPD and low SM lead to a reduction in ϕ_F. Helm et al. (2020) links the drought-induced decrease in ϕ_F to a decrease in Gs. At the satellite scale, fewer studies use ϕ_F in favour of SIF, that has shown to be reactive to drought conditions. Sun et al. (2015) linked different drought categories from the US drought monitor (Svadoba et al., 2002) to the ecosystem-scale SIF.

However, the SIF drought reaction is determined by a simultaneous canopy structural and physiological change (Dechant et al., 2020), the sum of which caused a SIF decrease that goes together with a GPP decrease (He et al., 2020). The combination of the structural and physiological components makes SIF a more performant drought diagnostic compared to greenness indices (Qiu et al., 2022). Recently, regional satellite-based studies have isolated physiological component and observed its reactivity to droughts (Gu et al., 2023; Zhang et al., 2023). The combination of the structural and physiological component makes SIF a more performant drought diagnostic compared to greenness indices (Qiu et al., 2022). The physiological component of SIF boils down to the fluorescence yield ϕ_F, a variable that is unaffected by canopy greennes or structure. Dechant et al. (2022) propose an efficient method for retrieving ϕ_F from satellite-based sensors, by normalizing the SIF. A global, satellite-based dataset of ϕ_F opens the door to an improved interpretation of SIF data through an ecophysiological lens.

Two environmental variables that stand out as constraining factors on the ecosystem-scale photosynthesis and SIF emission are water availability, typically quantified with the SM and the atmospheric water demand, quantified with the VPD (Fu et al., 2022; Lu et al., 2022). In order to interpret the control of VPD and SM on photosynthesis, and therefore on ϕ_F and SIF, it is important to consider the stomatal behaviour. The connection between Gs, ϕ_F and photosynthesis is well-established at the plant level (Flexas et al., 2002; van der Tol et al., 2014). The specific nature of this connection at the ecosystem level differs on a series of ecosystem properties, of which the isohydricity a key trait. Isohydricity is an ecophysiological trait that describes the sensitivity of the stomata to increasing drought conditions. A plant is more isohydric if its stomata are sensitive to drought (i.e., they tend to close in response to drought), and more anisohydric if the stomata are less sensitive (i.e., they tend to remain open despite of drought conditions). More isohydric plants save up water during drought periods at the cost of a lower carboxylation rate, while more anisohydric plants maintain high photosynthetic rates during drought periods, putting themselves under risk of hydraulic failure but potentially outperforming their more isohydric neighbours (Novick et al., 2019). Considering the environmental variables soil moisture (SM) and vapour pressure deficit (VPD), as well as the physiological variables Gs and ϕ_F at the ecosystem scale, we hypothesize that: (i) VPD and SM are important controlling factors on ϕ_F, (ii) as anisohydric plants are known to have a less strict stomatal response to changes in environmental factors, an effect of the anisohydricity is expected on the response of ϕ_F to VPD and

SM, (iii) the relationship between canopy conductance (Gs) and ϕ_F holds in a way it holds at the scale of the individual plant (e.g., Flexas et al., 2002). The paper is structured as follows. Section 2 explains the datasets used and the methodology, including the way we compute ϕ_F, the analysis of SM and VPD as controlling factors, and the modelling of stomatal conductance. Section 3 shows the results in four steps: (i) the spatial patterns of ϕ_F; (ii) the time-correlation between ϕ_F and greenness; (iii) the controls of SM and VPD on ϕ_F; and (iv) the comparison of the SM-VPD-ϕ_F space with the SM-VPD-Gs space. Sections 4 and 5 are the discussion and conclusions.

2. Materials and Methods

2.1. Data

2.1.1. L-band passive microwave soil moisture from SMAP

Passive microwave remote sensing at L-band (1.4 GHz) provides an excellent tool for monitoring soil moisture regularly and globally. Advantages of this technique include: (i) compared to higher frequencies, the longer wavelengths maximize the soil depth to which the signal is sensitive; (ii) clouds are transparent, allowing for all-weather retrievals and (iii) compared to active microwave techniques and to shorter wavelengths, L-band passive microwave emission is less affected by the canopy structure. The coarse spatial resolution of passive microwave SM retrievals is particularly suited for regional to global scale research. This study makes use of L-band SM data from the Soil Moisture Active Passive (SMAP) satellite (Entekhabi et al., 2010) retrieved using the Multi-Temporal Dual-Channel Algorithm (MT-DCA; Konings and Gentine, 2017; Feldman et al., 2021). The data come at a 3-day temporal resolution and 9 km spatial gridding.

2.1.2. Atmospheric data from AIRS

The evaporative water demand is monitored with the Atmospheric InfraRed Sounder (AIRS) instrument, on NASA's Aqua satellite, launched in 2002 (Aumann et al., 2003). This instrument measures the infrared radiance at 2378 spectral samples, located in three spectral regions of the thermal infrared. Along these bands, atmospheric trace gasses, like CO_2 and H_2O, have different absorption spectra. Using this information, AIRS retrieves a vertical transect of temperatures and atmospheric trace gasses concentrations at the global scale with a daily resolution (Aumann et al., 2003). This allows computing daily data of VPD (Eq. 1-2) based on the saturation water vapour pressure (e_{sat}; kPa), air temperature (T_{air}; ^{o}C) and the air relative humidity (RH; %).

$$e_{sat} = 0.61094 \cdot e^{\frac{17.625 \cdot T_{air}}{T_{air}+243.04}} \tag{1}$$

$$\text{VPD} = e_{sat} \cdot \left(1 - \frac{\text{RH}}{100}\right) \tag{2}$$

Both Sentinel-5P (used to retrieve SIF; see Section 2.1.3) and Aqua satellites have their overpass times at 13.30, minimizing the diurnal shift between the VPD and SIF measurements. AIRS provides daily atmospheric data at 1^{o} spatial resolution. Using linear interpolation, the 1-degree dataset is regridded to a 9 km Equal Area Scalable Earth version 2 (EASE-2) grid. When interpreting VPD at a large scale, it is important to realize that VPD, air temperature and solar irradiation are tightly interconnected and that a VPD effect is hard to distinguish from an irradiation or a temperature effect. We try to limit the effects of the lower resolution VPD by binning ϕ_F relative to SM and VPD conditions (see section 2.2.2). This approach enables us to use datasets of different resolutions, although higher resolution VPD would increase the number of unique SM and VPD pairs for binning. We think that AIRS VPD sufficiently covers large scale atmospheric dryness, and we have high enough sampling to isolate the VPD control on ϕ_F.

2.1.3. SIF and NIR data from TROPOMI

The SIF data were taken from the 'TROPOSIF' product (Guanter et al., 2021), that retrieves SIF emission at its 740 nm emission peak (in mW m^{-2} sr^{-1} nm^{-1}) from the TROPOMI sensor onboard the Sentinel-5P satellite. The product represents instantaneous SIF emission at the moment of the measurement. The retrieval uses the spectral fitting window between 743 and 758 nm and relies purely on solar Fraunhofer lines, reducing its sensitivity to atmospheric effects compared to retrieval methods that include the atmospheric absorption bands. For the SIF retrieval, the observed signal over the different bands is split into a smooth (true) reflectance signal and a fluorescence signal. The latter makes up for the difference between the true and apparent reflectance (i.e., the reflectance as observed by the satellite). The retrieval assumes cloud-free conditions. The same TROPOSIF product also provided the broadband top of atmophere (TOA) NIR radiances (NIR$_{\mathrm{RAD}}$; in mW m^{-2} sr^{-1} nm^{-1}). TROPOMI has a 16-day revisit time and a swath of 2600 km, allowing it to combine nadir and off-nadir measurements. This combination allows a daily global coverage. The spatial resolution of the data product goes up to 3.5 km x 5.5 km at nadir, while going down to 14.5

x 5.5 km off-nadir. Each data point in the TROPOSIF product contains a quality value, with penalties for high Solar Zenith Angle (SZA), a low average TOA $\mathrm{NIR}_{\mathrm{RAD}}$, an extreme value for SIF, or a high Viewing Zenith Angle (VZA). As a final quality control, the χ^2-value between the calculated and observed spectra is calculated, allowing to identify the retrievals that have been hampered by clouds. The calculated spectrum is the sum of the smooth (true) reflectance and the fluorescence. Following the recommendations laid out in Guanter et al. (2021), this study only selected TROPOSIF SIF and $\mathrm{NIR}_{\mathrm{RAD}}$ data that did not take any penal point from the beforementioned categories. In the TROPOSIF dataset, SIF values can be negative. These values are the result of the lack of ground-based calibrations, as well as of a series of noise introduced by the atmosphere. Negative SIF values were mainly reported over areas with only sparse vegetation. While negative SIF values are not physical, they do represent the regions with the lowest SIF emissions and deleting the negative SIF values would introduce a negative bias in the system. Therefore, the negative SIF values were considered in our analyses. The negative data comprised of 23% of the data.

2.1.4. NDVI data from MODIS

Information on the vegetation development comes from NDVI data, which were obtained from the MOD13C1 product (Didan, 2015). This product is derived from the MODerate Imaging Spectroradiometer (MODIS) on board of the Terra satellite. This product bins two 8-day composite surface reflectance granules into a 16-day period and is set out on a 0.05^0 grid. The product has a staunch quality control, removing any cloud-affected data. In a second instance, the data were spatially aggregated and temporally interpolated to form a global 9 km product at a daily resolution. This approach allows to get a smooth signal on the vegetation development that minimizes the cloud effects, that profoundly affect the NDVI retrieval. Table 1 gives an overview of all the used remote sensing products, as well as on their resolutions.

Table 1: Overview of used sensors and data products.

Variable	**Sensor**	**Spatial grid**	**Time step**	**Reference**
Soil Moisture	SMAP	9 km	3 days	(Konings et al., 2017)
NDVI	MODIS	0.05^o	16 days	(Didan, 2015)
VPD	AIRS	1^o	1 day	(Aumann et al., 2003)
$\mathrm{NIR}_{\mathrm{RAD}}$	TROPOMI	Up to 3.5 km x 5.5 km	1 day	(Guanter et al., 2021)
SIF_{740}	TROPOMI	Up to 3.5 km x 5.5 km	1 day	(Guanter et al., 2021)

2.1.5. Isolating the physiological component from SIF to create a global ϕ_F dataset

To convert satellite-based SIF to ecosystem-scale ϕ_F values, three multiplicative factors need to be considered (Jonard et al., 2020) (Eq. 3).

$$\mathrm{SIF} = \mathrm{PAR}{\cdot}\mathrm{fPAR} \cdot \phi_{\mathrm{F}} \cdot f_{esc} \tag{3}$$

The first term is the photosynthetically active radiation (PAR), that fuels the photosynthesis. The second factor is the fraction of this PAR that the leaves absorb (fPAR). Finally, there is the escape probability (f_{esc}), the probability of a re-emitted photon by PSII to reach the sensor. The non-physiological part of SIF, being the fPAR, PAR and f_{esc} can be grouped in the NIRvP variable (Dechant et al., 2022) as in Eq. 4.

$$\mathrm{NIRvP} \approx \mathrm{PAR}{\cdot}\mathrm{fPAR}{\cdot}f_{esc} \tag{4}$$

While SIF has very strict spectral retrieval requirements, NIRvP can be measured by using only the Normalized Difference Vegetation Index (NDVI) and the reflected radiance in the TOA part of the near-infrared ($\mathrm{NIR_{rad}}$), as shown in Eq. 5.

$$\mathrm{NIRvP} = \mathrm{NDVI}{\cdot}\mathrm{NIR_{rad}} \tag{5}$$

Finally, normalizing SIF by NIRvP provides an estimate for ϕ_F (Eq. 6), the fluorescence yield (Zeng et al., 2022):

$$\phi_{\mathrm{F}} \approx \frac{\mathrm{SIF}}{\mathrm{NIRvP}} \tag{6}$$

As an additional quality control on the TROPOSIF product, data points of ϕ_F with a NIRvP < 25 mWm^{-2}sr^{-1}nm^{-1} were not considered, as they represent too small vegetation or too low solar radiations.

2.2. Evaluating the effect of environmental factors on ϕ_F

2.2.1. Grasping the spatial and temporal variation of ϕ_F

The analysis was based on data from the years 2019 and 2020. Three steps were made to explore the behaviour of ϕ_F along the spatial and temporal dimensions. First, a pixel-averaged map of global yearly ϕ_F was made for the year 2019. Second, to verify that the ϕ_F indeed represents effects that are unrelated to canopy-greenness, the pixel-based Pearson's correlation coefficient betweenϕ_F and NDVI was calculated for the year 2019. Third, to visualize the effect of a drought stress on large-scale ϕ_F, a ϕ_F map of Western Europe was made before and during the 2019 European Summer Drought (Blauhut et al., 2022).

2.2.2. Evaluating the effect of SM and VPD in a phase space

As a next step, we analyse the effect of the environmental variables SM and VPD on ϕ_F by plotting each observation of ϕ_F values in function of its corresponding VPD and SM observations in a phase space. While plant drought stress is a complex and multi-dimensional problem, SM and VPD represent respectively the supply and demand of water. Each point in the phase space considers a specific set of environmental conditions, i.e., a VPD-SM combination, and shows the average ϕ_F value for these conditions. The observed ϕ_F values over the years 2019 and 2020 were binned based on both their SM (55 bins, between 0 and 0.55 m^3/m^3, bin width 0.01 m^3/m^3) and

VPD (40 bins, between 1 and 5 kPa, bin width 0.1 kPa). To ensure statistical representativeness, we took global data over two years, and SM-VPD bins that contained fewer than 1200 measurements were removed. Within the phase space, contour lines connect points of equal ϕ_F. The shape of these lines qualitatively reveals the controlling factor on ϕ_F .

The analysis of phase space plots is done in two steps. In a first instance, a global average of the relationship between SM-VPD and ϕ_F is made through a phase space. The global analysis has the advantage of containing a maximal number of observations, but it neglects spatial variations in the response of ϕ_F to SM and VPD. In a second instance, the vegetation are considered, by plotting different phase spaces for each different land cover and isohydricity categories.

2.2.3. Data stratification of the global ϕ_F dataset with land cover, isohydricity

Mechanistically linked to photosynthesis, plant-scale ϕ_F is sensitive to plant isohydricity (Attia et al., 2015; Cocozza et al., 2016), although the precise relationship at ecosystem scale is unclear. The global ϕ_F dataset was stratified based on the degree of anisohydricity of each pixel (Table 2) using a global database of isohydricity from (Appendix A.1; Konings and Gentine, 2017). This dataset quantifies an ecosystem isohydricity based on the diurnal variation on satellite AMSR-E observations of X-band Vegetation Optical Depth (VOD), a proxy for the water potential in the leaves. This variation is quantified as the slope (σ) of the linear regression between daytime and night-time VOD. Pixels showing little σ values ($\sigma \sim 0$) were considered as more isohydric, meaning they have a strict stomatal control, therefore low diurnal VOD variation. Pixels with a σ values close to 1 were instead consid-

Table 2: Isohydricity classes, based on the slope between midday and midnight vegetation optical depth σ (Konings and Gentine, 2017).

Strictly Isohydric	**Isohydric**	**Rather Isohydric**	**Rather Anisohydric**	**Anisohydric**	**Strictly Anisohydric**
0—0.2	0.2—0.4	0.4—0.6	0.6—0.8	0.8—1	1—1.2

ered more anisohydric. Those pixels typically have higher daily transpiration rates, and therefore a larger difference between daytime and nighttime VOD (Konings and Gentine, 2017). While some ecosystems are reported to have a seasonality in their degree of anisohydricity, driven by leaf phenology (Gong et al., 2022), or due to species turnover (Wu et al., 2021). Studying time-variable effects of isohydricity is beyond the scope of this study. Isohydricity is thefore considered as a time-constant value. To assess the effect of isohydricity and anisohydricity on the ϕ_F under different SM and VPD conditions, we split ecosystem-scale isohydricity into 6 discrete classes.

In addition to the isohydricity effect, the effects of land management were studied. To do so, croplands were treated distinctly from other vegetation types as they typically show a clear anisohydric behaviour and farming practices allow agricultural crops to grow optimally, with high photosynthetic rates. Such management practices are not present in natural ecosystems. The vegetation type information come from the International Geosphere–Biosphere Programme (Friedl et al., 2010) land cover classification information. Both the land cover and isohydricity analyses were carried out over the global dataset.

2.3. Modelling Gs at the continental scale

SM and VPD affect ϕ_F through partially driving stomatal closure (Jonard et al., 2020), as closed stomata limit the plant's carboxylation rate. Therefore ϕ_F and Gs should be controlled by SM and VPD in similar ways. We test this by comparing ϕ_F observations to Gs model estimates. We do not attempt to validate ϕ_F using Gs but aim to explore whether both variables are controlled by SM and VPD in similar ways and whether a previously observed relationship between ϕ_F and Gs is reproducible using continental scale ϕ_F and model estimates (Flexas et al., 2002). Similar comparisons have been done by Zhang et al. 2021, Fu et al. 2022 and Liu et al. 2020, although on smaller scales. Work by Zhang et al. (2021) relies on Gs calculated using the Penman Monteith equation, which requires substantial local measurements to parameterize the model properly. The Gs data we use is based on a simple soil-plant hydraulic model, originally designed by Carminati and Javaux (2020) and expanded by Wankmüller and Carminati (2021). We run the model with remote sensing observations of SM and VPD (same as in Table 1) as inputs to predict Gs for Africa. Furthermore, Soil hydraulic properties are calculated using empirical formulations by Rawls and Brakensiek (1985) and global soil maps (Hengl, 2018a,b) and root length is adjusted as a fraction of MODIS leaf area index (LAI). Limiting the scope of the analysis to the African continent reduces the computation time to a manageable amount, while still analysing a large diversity of different biomes and climates. Due to the coarse input datasets and the computationally expensive nature of the model, we estimate Gs at 36 km resolution.

The plant soil hydraulic model we use has been desrcibed in Carminati and

Javaux (2020) and Wankmüller et al. and includes radial water transport from soil to root, which is often not resolved in larger ecosystem models. The model operates under the steady state assumption, i.e., all water fluxes equalize between soil and plant compartments. Water flow between soil and plant follows from the water potential difference between compartments and the compartment conductance. The decrease of soil conductance as a result of root water uptake is nonlinear and can quickly limit the conductance of the whole soil plant system in dry conditions, which might exert strong control on stomatal response (Carminati and Javaux, 2020). The model setup does not prescribe species specific traits or levels of isohydricity. The relationship of Gs to SM and VPD is resulting from the models' soil and plant hydraulics and the local SM and VPD time series. Our goal is to provide a simple comparison between SM and VPD control on ϕ_F and plant hydraulics-based Gs. Abscisic acid (ABA) is a plant hormone relevant for many plant processes, like growth, and a plays an important role in signalling water stress. It has been observed that increasing ABA levels lead to stomatal closure, therefore reducing plant water loss (Bauer et al., 2013). Wankmüller and Carminati (2021) include the effect of ABA on stomatal/canopy conductance using following simple model. The relative level of ABA (-) follows from a sink-source equation (Eq. 7):

$$|ABA| \propto \frac{-\Psi_{\text{leaf}} + \epsilon_{\Psi}}{A + \epsilon_A} \tag{7}$$

where the source term in the numerator depends on the leaf water potential Ψ_{leaf} (MPa) and a constant minimum production rate ϵ_{Ψ} (MPa). The sink term in the denominator depends on an assimilation rate A and a constant minimum degradation rate ϵ_A (μmol m^{-2}s^{-1}) . ψ_{leaf} results from the solution of the plant hydraulics model for a given transpiration rate Eleaf. This description of ABA dynamics is extremely simplified, not including a variety of other factors and processes, like the transport of ABA in the plant or the dependence of ABA production and degradation on temperature, among others. The assimilation rate A μmol m^{-2}s^{-1} is modelled as a function of stomatal conductance and a saturation curve (Eq. 8:)

$$\mathrm{A}\left(\mathrm{G_S}\right)=\frac{\frac{\mathrm{G_S}}{1.6}\mathrm{A_{max}}}{\frac{\mathrm{G_S}}{1.6}+\mathrm{K_M}} \tag{8}$$

where $\mathrm{A_{max}}$ (μmol m^{-2}s^{-1}) is the maximum assimilation rate and K_M(μmol m^{-2}s^{-1}) is the Michaelis-Menten constant. $\mathrm{G_S}$ (μmol m^{-2}s^{-1}) linked to the transpiration rate using the following simple model (Medlyn et al., 2011):

$$\mathrm{G_S}=\mathrm{TA_{leaf}}\frac{\mathrm{P_{atm}}}{\mathrm{VPD}} \tag{9}$$

with transpiration rate $\mathrm{E_{leaf}}$, $\mathrm{P_{atm}}$ the atmospheric pressure and VPD the vapour pressure deficit. Equation 9 displays the dependence of Gs, and therefore of |ABA| on plant hydraulics (through $\mathrm{E_{leaf}}$) and VPD. Furthermore, Ψ_{leaf} goes into equation (7) which influences |ABA| and subsequently Gs as well. The whole model containing plant hydraulics and ABA dynamics is iteratively solved by minimizing |ABA|, which results in an estimation of Gs for every timestep with SM and VPD observation. We refer to Carminati and Javaux (2020) and Wankmüller and Carminati (2021) for a more detailed description of the model framework and provide our exact parameterization in the supplement. The model framework does not include any functional dependence of Gs on light availability or temperature, which should limit the ability of the model to capture Gs dynamics in areas where they are most important and water limitation is not relevant (e.g rainforests).

3. Results

3.1. Global patterns of ϕ_F

Figure 1 shows the global average ϕ_F for 2019 at 9 km resolution. Regions that typically show a clear moisture gradient, such as the Sahel region or Northern Australia, tend to show a gradient in ϕ_F. Western Europe, India, Brazil, Tropical Africa and Southeast Asia show high values of ϕ_F. Smaller-scale patterns however, are harder to spot.

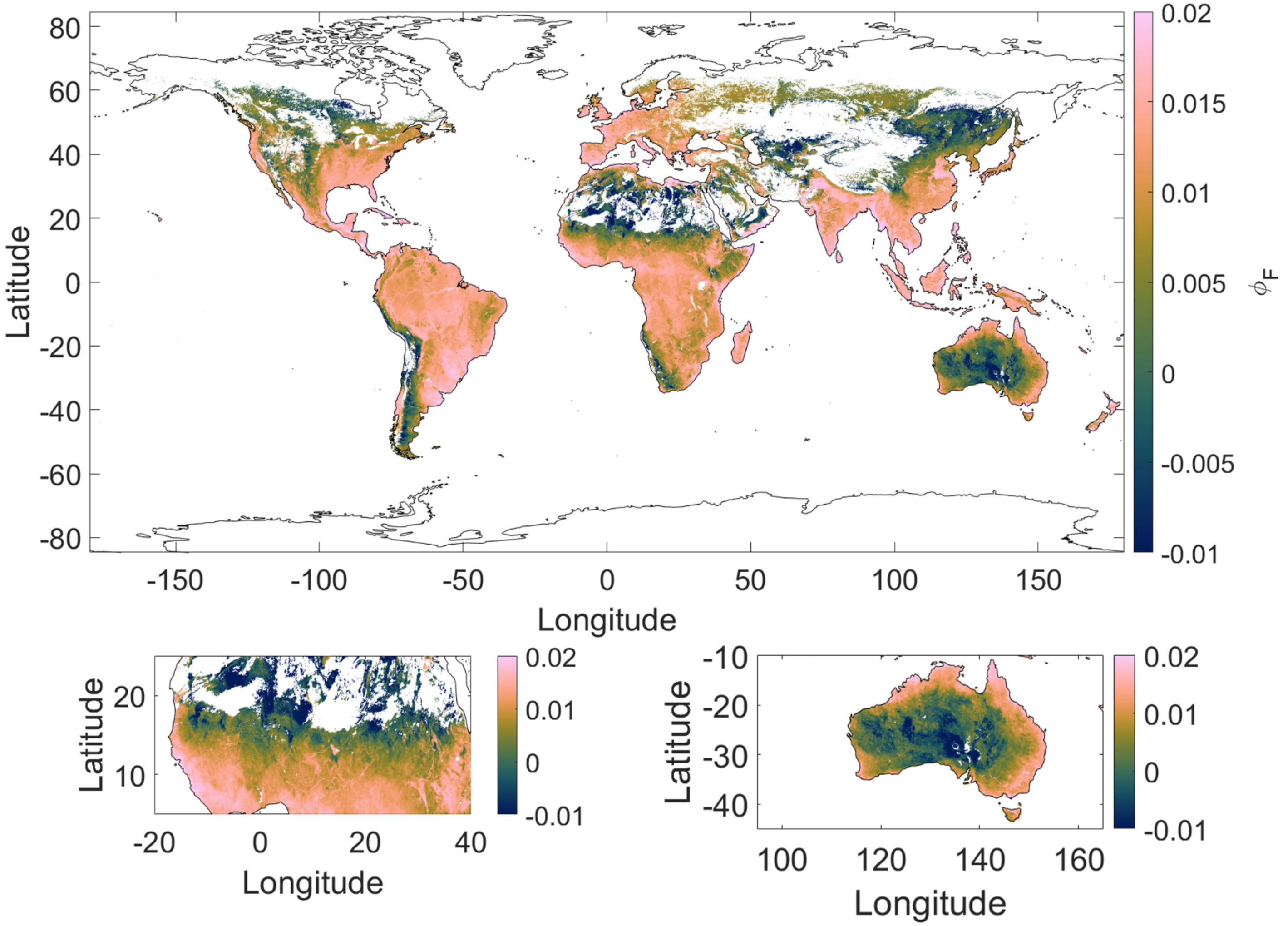

Figure 1: Pixel-averaged global distribution of ϕ_F for 2019, with zoom-ins on the Sahel (bottom left) and Australia (bottom right).

In addition to the spatial patterns, the ϕ_F also shows reactivity to disturbances, that typically reduce the ϕ_F. This concept is illustrated by Figure 2, which shows the ϕ_F over Western Europe during a regular 2019 spring (Figure 2a) and the First European heatwave 2019 (Figure 2b) in Western Europe (Blauhut et al., 2022). The map shows a clear decrease in ϕ_F in France and Southern Germany (Figure 2c). This behaviour was not repeated in 2021, a year in which heatwaves and droughts were absent in Europe.

Figure 3 shows the pixel-based Pearson's correlation coefficient between NDVI and ϕ_F ($\rho_{\phi_F\text{-NDVI}}$) for 2019. Spatially, regions with a high ϕ_F-NDVI correlation tend to concentrate in regions that have either a semi-arid climate, such as the Sahel, or that are situated at high latitudes, such as Siberia or Canada. The histogram of the correlation coefficient shows a clear peak around 0, indicating that the ϕ_F is unrelated to the NDVI for most pixels. Significant (p-value < 0.05) NDVI-ϕ_F correlations grouped around the sahel and the Taiga regions in Canada and Siberia (Figure Appendix A.4).

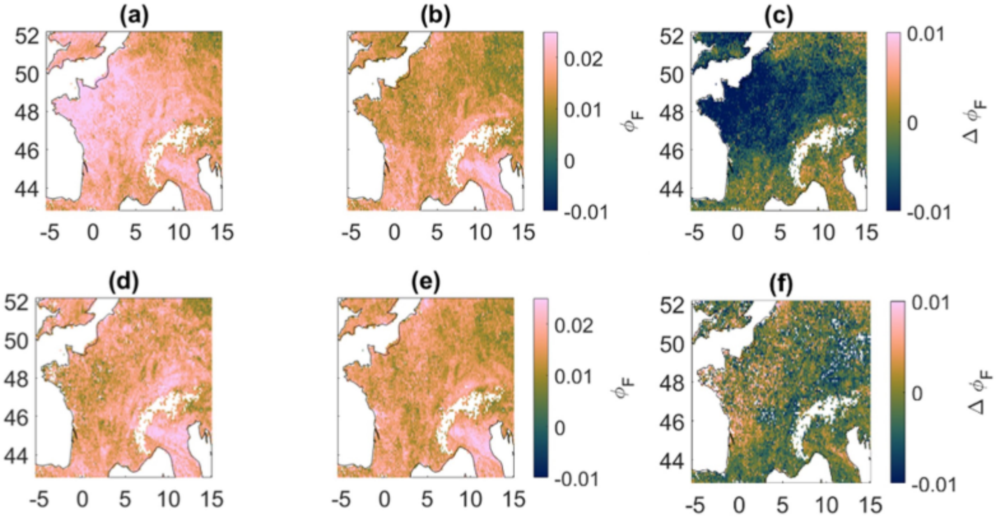

Figure 2: (a) Spatial overview of the average ϕ_F for June 1^{st}-June 11^{th} (b) Spatial overview of the average ϕ_F for June 25^{th}-July 5^{th}, the 2019 European heatwave; (c) difference in ϕ_F between Figures (a) and (b). (d), (e) and (f) show the same periods of the year, for the year 2021, a wet year.

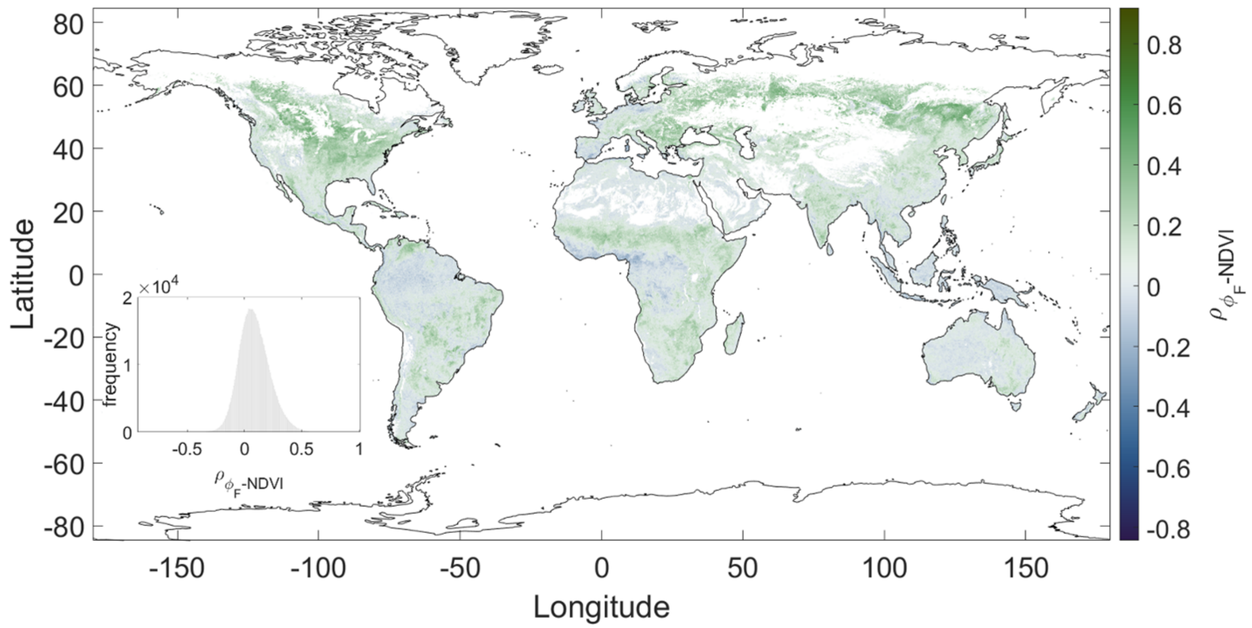

Figure 3: Global map of the ϕ_F-NDVI based Pearson's correlation coefficient for 2019.

3.2. Observed control of SM and VPD on ϕ_F

Figure 4 shows the global ϕ_F as a function of the SM and VPD. Considering almost all global terrestrial ecosystems, figure 4 shows a general image on the behaviour of ϕ_F over the globe. The highest ϕ_F values are found in the VPD range between 2 and 3 kPa. Some SM-VPD combinations were more frequent than others, which is represented by Figure 4b. For the region with VPD $<$ 1.8 kPa, the horizontal contour lines indicate that VPD is the only driving factor for the ϕ_F. For the region with VPD $>$ 1.8 kPa, the more curved and diagonal contour lines indicate a co-regulation of ϕ_F by SM and VPD, especially for VPD $>$ 2.5 kPa. Figure 4c shows in another way that VPD is the main factor driving ϕ_F for the region VPD $<$ 1.8 kPa. For higher VPD, a decrease in soil moisture leads to a decrease in ϕ_F. This is most for the region SM > 0.25 m^3/m^3 , which is also visible in the right part of Figure 4a. Figure 4b shows points with a higher SM tend to be more frequent in the lower VPD part and vice versa. Therefore, high SM-high VPD points were excluded from the analysis. Figure 4c shows clearly the control of VPD on ϕ_F at lower VPD values and the role that SM plays in this control at higher VPD.

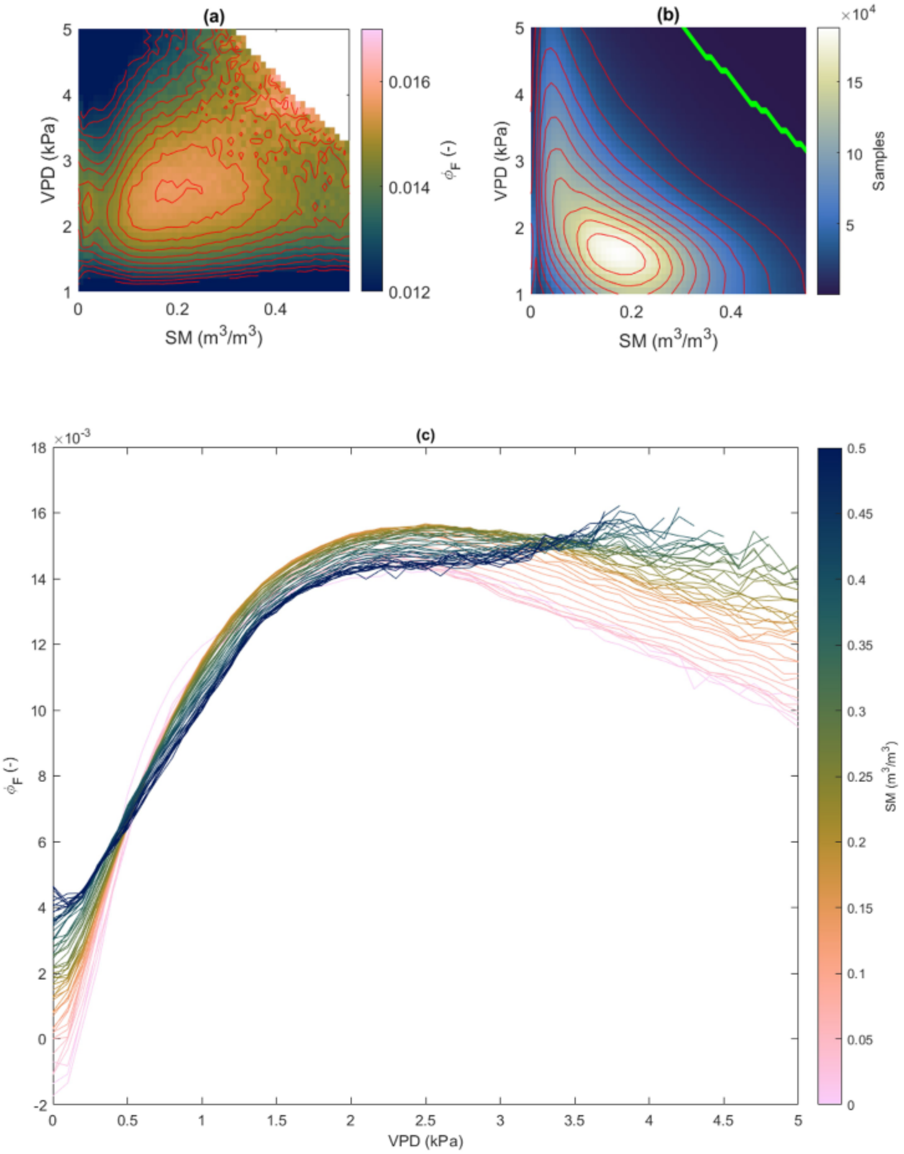

Figure 4: (a) phase space showing the average ϕ_F for each SM-VPD combination that emerged from a global analysis during the years 2019 and 2020. The red lines denote contour lines of regions of equal ϕ_F values. (b) Number of samples for each SM-VPD combination. The green line in Figure b shows the threshold of 1200 combinations; and fewer combinations (i.e., right of the line) are removed from the analysis. (c) represents the same data as (a), but the axes are swapped.

3.3. Isohydricity modulates control of SM and VPD on ϕ_F

Figure 5 shows the ϕ_F values in function of both the SM and VPD conditions along the isohydricity strata. All the subplots replicate the global behaviour, with maximal ϕ_F values found in the region of VPD between 2 and 3 kPa. The ϕ_F behaved similarly in the classes isohydric, rather isohydric and rather anisohydric. In contrast, in the two most anisohydric categories (isohydricity < 0.2), the ϕ_F values were notably higher than in the more isohydric classes. In addition, there was a clear local maximum for SM around 0.17 and VPD around 2.2 kPa, for the rather anisohydric and anisohydric classes. This local maximum was not observed for the more isohydric classes. In the most anisohydric class, the ϕ_F was almost completely decoupled from the water availability, with a decrease in ϕ_F only setting in when the SM values approach to 0.

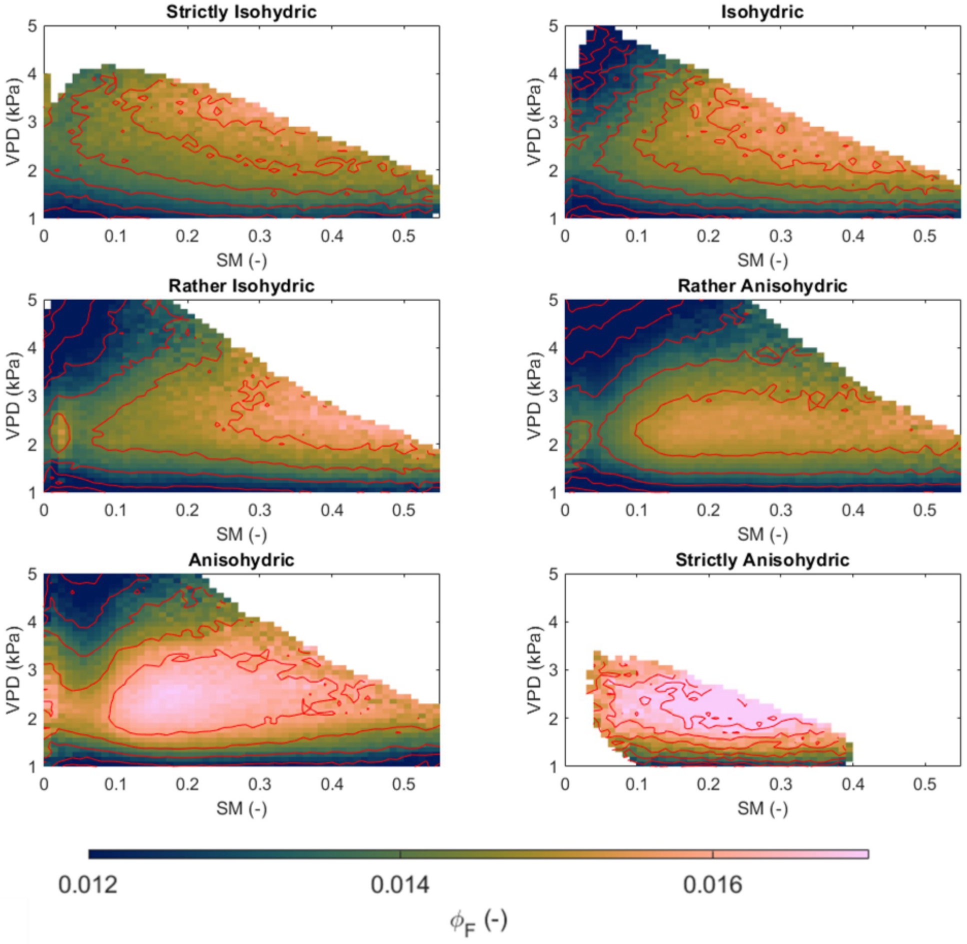

Figure 5: Phase spaces of the ϕ_F values along the SM-VPD space for six different isohydricity classes.

Figure 6 shows the effect of increasing VPD on the ϕ_F under ranges of averaged soil moisture conditions for the different isohydricity classes. The figure shows a very clear difference in the ϕ_F emission for the VPD range between 1 and 3 kPa. For VPD $>$ 2.5 kPa, the ϕ_F tends to decrease in response to a higher VPD. Consistent with Figure 5, there is an increasing trend of ϕ_F with increasing isohydricity, and very anisohydric regions show the highest ϕ_F values, especially for VPD above 1 kPa. It is worth noting that the more isohydric ecosystems show a higher ϕ_F at VPD < 0.8 kPa. For the lower SM classes, the isohydricity effect on ϕ_F is more notable, as the two more anisohydric lines clearly show the highest ϕ_F value in the plot with the lowest soil moisture in the region with VPD > 0.8 kPa. In contrast, the plot with SM > 0.45 m^3/m^3 shows that the isohydricity almost plays no effect on ϕ_F, except for the most anisohydric category.

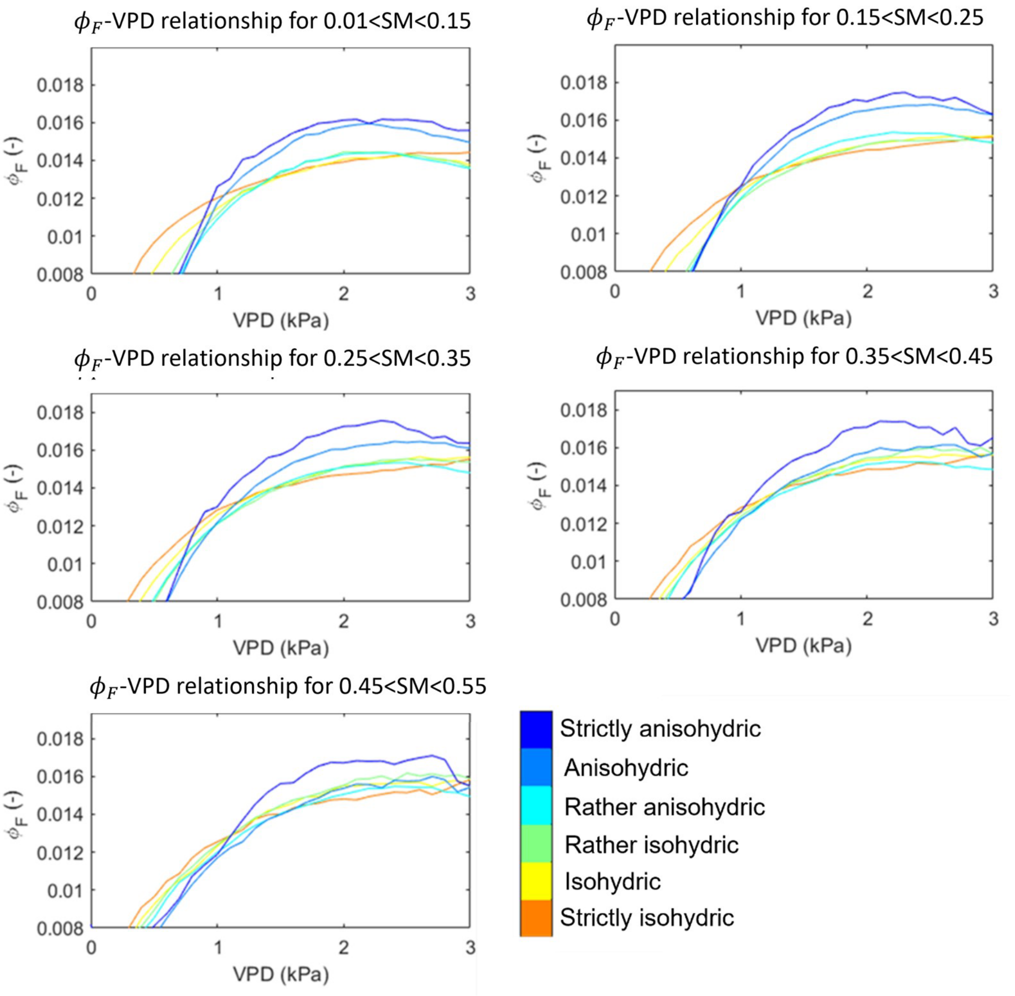

Figure 6: ϕ_F-VPD relationship at different soil moisture condition ranges and isohydricity classes. Values for VPD>3 kPa were not shown, as there were too few observations in this class.

Croplands tend to behave differently in their SM-VPD space compared to other vegetation (Figure 7). As a main difference, the croplands show higher ϕ_F values compared to the non-croplands, while the shape of the contour lines does not change significantly. It should be noted that the cropland vegetation contains a higher proportion of more anisohydric pixels (mean of 0.4 for non-croplands, mean of 0.2 for croplands, Figure Appendix A.2).

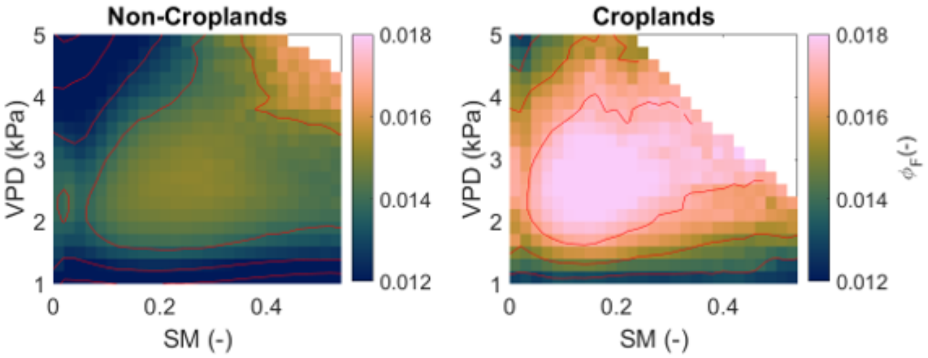

Figure 7: Phase space of ϕ_F along the SM-VPD space for croplands and non-croplands (i.e., other vegetation types that are not croplands).

3.4. Comparison of ϕ_F observations and modelled Gs at the continental scale

Figure 8 shows the phase space and contour plot of ϕ_F and Gs. The main similarity between the ϕ_F and Gs phase space is that they both decrease with decreasing SM conditions, but the ϕ_F decreases are less steep compared to the Gs decrease. Overall, both show a similar VPD-dominated regime at high SM and a co-regulated regime at low SM. For SM < 0.15 m^3/m^3, the Gs lines are close to vertical along the entire VPD range. This behaviour is not presented in the ϕ_F data. ϕ_F at low SM might pick up adapted dryland vegetation, which is not represented in the trait-less model. For the low VPD range, modelled Gs does not increase with VPD, which is likely due to the limitation that Gs is only driven by water limitation (i.e., SM and VPD) but is not an explicit function of temperature or light. Future adaptation to the Gs model could include these effects and might make the model more realistic.

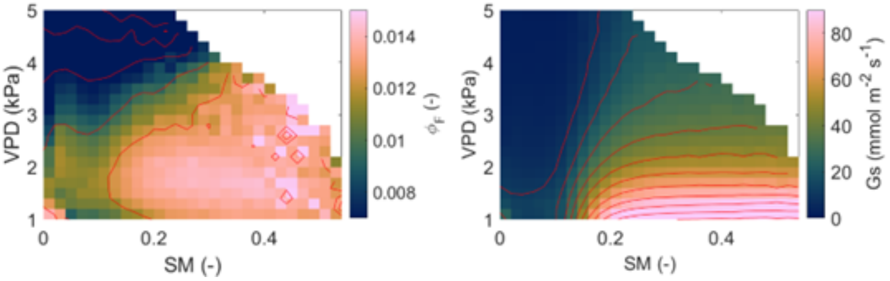

Figure 8: ϕ_F (left) and Gs (right) values over the African continent during 2019-2020 in the SM-VPD phase space. The ϕ_F dataset was re-gridded to 36 km before being put in the phase space. The minimal threshold for an SM-VPD combination to be included in the plot was at 120 samples.

Leaf-scale observations on fluorescence yield and stomatal conductance have shown a concave relationship, in which the ϕ_F approaches a maximal value for high Gs values. The ϕ_F-Gs curve showed a concave relationship (e.g., Flexas et al., 2002). The same behaviour is replicated in Figure 9, despite of being made at the continental scale. The low Gs-region in this figure can be approximated with a linear curve. This is also the region where SM and VPD are the most constraining factors on ϕ_F. When looking at the map of the pixel-based Pearson's correlation coefficient of ϕ_F and Gs (Figure 10), the strongest correlation between Gs and ϕ_F is found in the Sahel region as well as in East Africa, but overall observed ϕ_F and modelled Gs show reasonably high correlations in most water-limited areas. A low and negative correlation between ϕ_F and Gs can be found in some parts of the Ethiopian Highlands as well as in the Congolese Rainforest, both regions where light and temperature might be the dominant controls on ϕ_F.

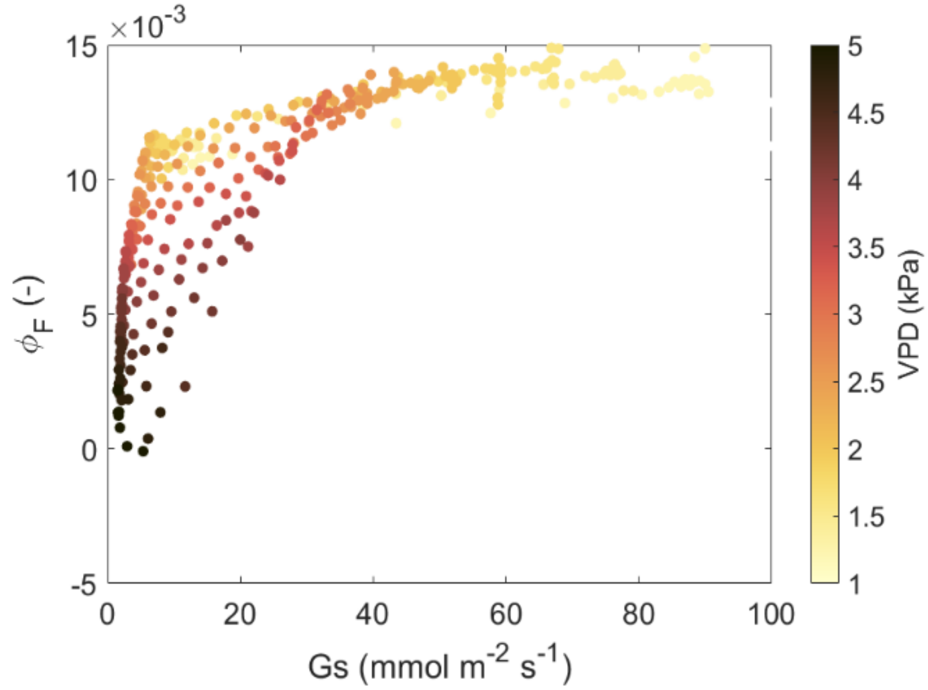

Figure 9: ϕ_F values from the SM-VPD space over the African continent during 2019-2020 (Figure 8) plotted in function of the Gs value and SM in the colourbar. Each dot represents the ϕ_F average over the considered SM-VPD bin.

A significant correlation coefficient was found all over Sub-Saharan Africa, albeit scattered around (Figure Appendix A.3.

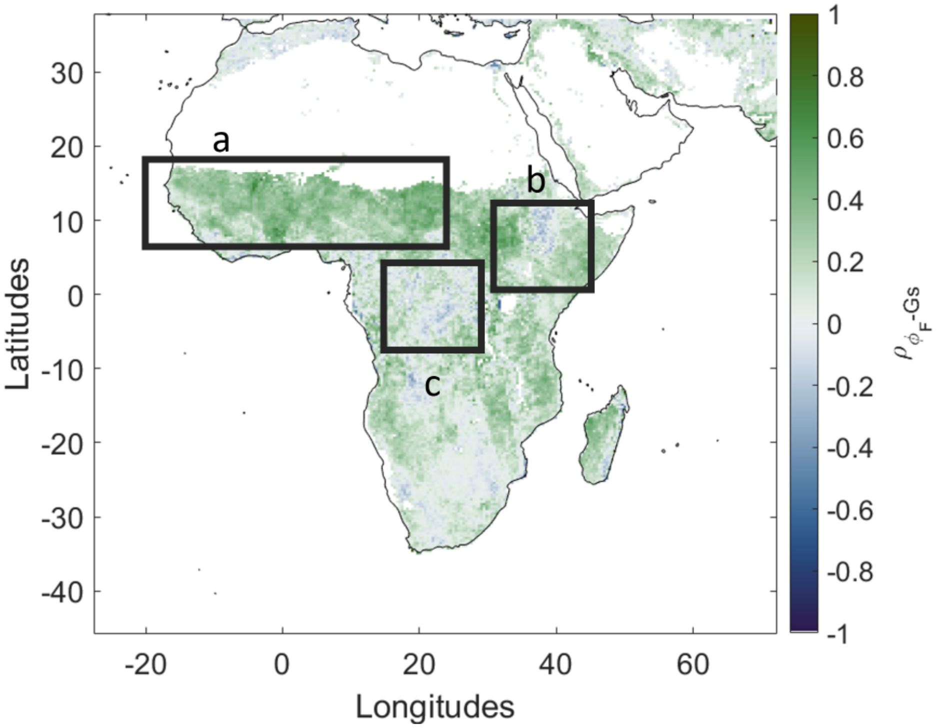

Figure 10: Pixel-based correlation between Gs and ϕ_F over Africa during the years 2019 and 2020. Data points with a VPD < 1.5 kPa were excluded from the analysis, to ensure that light-limited photosynthesis is excluded. a: denotes the Sahel regions; b: denotes the Ethiopian Highlands and C: denotes the Congo River Basin.

4. Discussion

4.1. Interpretation of spatial patterns in global ϕ_F data

The different phase spaces (Figure 4-8) show that the ϕ_F is sensitive to the soil, plant and atmospheric characteristics. These sensitivities are consistent with the spatial gradients of ϕ_F that appear in figure 1. Clear examples here are the increase in ϕ_F over the Sahel region or in the Australian Outback, where the ϕ_F decreases gradually when entering the desert zone. In addition, in some mountain areas such as those in the Western United States, ϕ_F is lower because high altitude regions tend to show a lower photosynthetic activity (Fujimura et al., 2010). Low ϕ_F values are mainly found in regions with either sparse vegetation, like the Australian Outback, or very low irradiations, such as Siberia. In such regions, a low SIF value is also expected.

The low correlation coefficient between NDVI and ϕ_F (figure 3) shows that ϕ_F and NDVI are fundamentally different, strengthening the case that satellite-based ϕ_F indeed represents the physiological component of the SIF emission independently of vegetation greenness. Figure 3 shows only two situations in which NDVI and ϕ_F tend to be correlated. The first is in regions with high latitudes. There, high VPD values are rare, so ϕ_F tends to show a seasonality with high ϕ_F in summer and lower in winter, which is similar to the typical NDVI seasonality. Both are driven by limitations in temperature and irradiation which are found at high latitudes. The second situation where NDVI and ϕ_F show a high correlation is in regions where plants tend to shed or brown their leaves in the dry season, such as the Sahel region (Tagesson et al., 2015), where a strong water limitation is expected. This is consistent with Jonard et al. (2022), who identified a strong coupling between light availability and sun-induced chlorophyll fluorescence tended to show a high ϕ_F-NDVI correlation coefficient.

4.2. Global-scale interpretation of ϕ_F

4.2.1. Constraining effect of SM and VPD on ϕ_F *at the glocal scale*

While SIF data have proven their ability to detect drought stress, especially drought onset, at the regional to global scales (e.g., Cao et al., 2021; Sun et al., 2015), the effects of irradiation and vegetation structure (the latter changing f_{esc}) might overpower ϕ_F (Dechant et al., 2020; Ryu et al., 2019; Yang and van der Tol, 2018). The structural effect include short-term variation in f_{esc} as a result of changes in leaf turgor (Xu et al., 2021) or due to wind effects (Liu et al., 2020). In addition, prolonged stress leads to a lowered NDVI, an effect that persists after the stress period (Wong et al., 2021), which provides an additional difficulty in interpreting SIF data. Working on ϕ_F comes with the advantage that it is stripped of non-physiological effects.

Acknowledging the importance of the structural changes on the escape probability, regional-scale studies using satellite-based SIF data have shown that variation in ϕ_F has its value in drought monitoring, thanks to the sensitivity of ϕ_F to the efficiency of the photosynthetis (Gu et al., 2023; Kimm et al., 2021b). In the latter studies, the reaction of ϕ_F to a drought is shown in a way similar to Figure 2. A quantitative analysis of the effect of a dry soil and a high vapour pressure deficit on photosynthesis shows a reduction on photosynthetic activity under high VPD or low SM (Sulman et al., 2016; Novick et al., 2016). The phase spaces in our study show a similar decrease in ϕ_F depending on SM and VPD. This suggests that ϕ_F bears the potential of being a tool for evaluating plant functioning under changing water availability and demand.

The changes in ϕ_F according to SM and VPD variability are similar to those occurring in Gs, as shown in Figure 8. This suggests that the link between Gs and ϕ_F, as described at the leaf scale (Flexas et al., 2002) or at the canopy scale (Kimm et al., 2021a) holds at the global scale. Gs is known to be constrained by a combination of SM and VPD, both at the ecosystem (Novick et al., 2019) and the local level (Zhang et al., 2021). A similar result is obtained for photosynthesis as such (Fu et al., 2022). This result is consistent with the concept of light- and water-limitation in ecosystem-scale photosynthesis (Jonard et al., 2022), since water limitation is assumed to induce a reduction in Gs through stomatal closure. As low irradiation values typically go together with low VPD values, the increase in ϕ_F at low VPD is likely an irradiation or a temperature effect.

There is a significant landscape-scale interaction between SM and VPD, as a high VPD (i.e., dry air) tends to dry out the soil (Liu et al., 2020), and dry/wet soils have also the capacity to reinforce dry/wet atmospheric conditions. These interactions explain why some SM-VPD combinations are more frequent than others, and why the high SM-high VPD combination is so rare (Figure 4b). In this sense, the co-regulation of SM and VPD on ϕ_F, reported in Figure 4, can also represent a downstream effect of the dry air drying out the soil, or vice-versa. Determining whether SM or VPD (water availability or atmospheric water demand) is the main driving factor on the changes in ϕ_F would require further assessment on how SM and VPD are interrelated both in space and time (Feldman et al., 2020).

While the satellite-based ϕ_F data and the modelled Gs provide one single value for large areas, local-scale studies have reported significant within-field and within-plant variability of ϕ_F or SIF emission. This high degree of spatial variability finds its origins in spatial differences in stress and irradiation conditions (Pinto et al., 2016; Wieneke et al., 2016; Zeng et al., 2022). In addition to small-scale spatial variations in environmental factors, plants can have different biotic traits such as isohydricity and heat resistance. Both show a variation at the level of the individual plant (Bussotti et al., 2020; Pinto et al., 2016; Wu et al., 2020), while the phase spaces in this study (Figure 4-8) show the global controls of VPD and SM on ϕ_F. Future work should address specific analyses in the spatial and temporal domains. Such studies can answer whether the relationship behaves similarly in space and time.

4.2.2. Role of non-photochemical quenching at the global scale

The most direct way to establish a link between ϕ_F and Gs is to make leaf-scale measurements with a fluorometer and a leaf chamber. A milestone study in this regard was Flexas et al. (2002), that observed a hyperbolic relationship between ϕ_F and Gs, where ϕ_F, as well as the photosynthetic rate, decrease with decreasing Gs. In the presented study, a similar relationship was found between TROPOMI ϕ_F and modelled Gs (figure 10). Helm et al. (2020) expanded this idea by comparing leaf-scale spectrometer SIF measurements with stomatal conductance measurements, and they found a similar connection between ϕ_F and Gs. Both studies attribute the decrease in ϕ_F or SIF to an observed increase in NPQ. While it makes sense to believe that the increase in NPQ is also responsible for the decrease of satellite-based ϕ_F at the global scale, it is impractical to verify this claim, as there is currently no reliable method for estimating NPQ from a remote sensing platform. The closest we have to a remote-sensing based NPQ estimate comes from the PRI. Short-term PRI dynamics are closely linked to NPQ dynamics. Using airborne imagery over an orchard, Zarco-Tejada et al. (2012) observed a simultaneous decrease in SIF, PRI and Gs, strengthening the case that the drought-induced decrease in canopy-scale SIF might indeed be driven by a decrease in Gs and an increase in NPQ. While the link between NPQ and ϕ_F at the global scale remains speculative, it is important to consider NPQ in the interpretation of ϕ_F under water-limited conditions, since the NPQ component forms a key element in linking ϕ_F to ecosystem-scale photosynthesis (Lee et al., 2015; Qiu et al., 2018).

4.3. Advantage of ϕ_F over other remote sensing signals

Optical remote sensing measures mainly the greenness and near-infrared reflectance signatures of the vegetation, which then is linked to the vegetation health as prolonged soil moisture deficit is reducing the canopy greenness. However, these techniques fail to capture more immediate effects of water limitation or stress. To do so, a variable that reacts instantly and in accordance to the stress intensity is useful. Along with ϕ_F measurements, two other techniques are indicative of environmental constraints on photosynthesis. These are the photochemical reflectance index (PRI) that is sensitive to the NPQ component in PSII and indicators that make use of thermal remote sensing. PRI is driven by the stress-induced increase in ϕ_N, making its driving factors similar to the factors driving ϕ_F (Acebron et al., 2021; Alonso et al., 2017). However, the interpretation of the PRI is blurred by the presence of bare soil or by the canopy structure (Yang, 2022). Synergetic use of PRI and ϕ_F data is expected to lead to a better description of the energy splitting at the level of PSII. Thermal remote sensing-based stress detection relies on the decrease in latent heat flux over the leaves because of reduced gas exchange. The reduction in the latent heat flux leads to an increase in the sensible heat flux and thus in an increase in leaf temperature (Maes and Steppe, 2012). This effect can be used to constrain the plant resistances, which allows for better modelling of the plant water and carbon fluxes (Bayat et al., 2018). Another thermal-based technique is the crop water stress index (CWSI), which compares the measured canopy temperature to a wet and dry reference (Berger et al., 2022). These variables are notoriously hard to measure, resulting in significant errors over global CWSI-based stress monitoring.

From this perspective, global ϕ_F is a promising variable that is linked in a more physiologically established way to Gs, reducing the need for ancillary data in its interpretation. Specifically, ϕ_F is mechanistically coupled to the PSII activity, allowing ϕ_F to constrain photosystem activity-related parameters in photosynthesis models. However, this comes at the cost of very strict spectral retrieval requirements. Consequently, ϕ_F comes with a coarse spatial resolution and significant instrument noise.

4.4. Consistent behaviour of ϕ_F *and Gs at the continental scale*

Since ϕ_F carries is controlled by SM and VPD, ϕ_F is a promising variable for constraining photosynthetic electron transport at the global scale. At the leaf level, ϕ_F is mechanistically coupled to the PSII activity, allowing ϕ_F to constrain light-harvesting-related parameters in photosynthesis models. The consistency between the hyperbolic shape in figure 10 and the shape obtained by the leaf-scale study of Flexas et al. (2002) and by the regional-scale study of Kimm et al. (2021b) suggest that the observation from the leaf scale on the link between Gs and ϕ_F might be useful for a solid ecosystem-scale link between ϕ_F and photosynthesis under water limitation. There are various hurdles to take before mechanistic-based land surface models can exploit this link. The first hurdle is linked to the strict spectral requirements for SIF retrieval and the instrument noise. The second hurdle deals with the upscaling of the link between ϕ_F, NPQ and Gs. Given the link between photosynthesis and crop yield, satellite-based SIF has already improved the crop yield predictions (Guanter et al., 2014). Further exploring the link between ϕ_F, photosynthesis, Gs and crop yield will improve the estimations of crop yield under water-limited conditions.

4.5. Perspectives for the FLuorescence EXplorer (FLEX) mission

While the TROPOSIF data are encouraging for presenting SIF's ability to detect environmental constraints on photosynthesis, the first satellite designated for SIF measurements is scheduled for launch in 2025. The Fluorescence Imaging Spectrometer (FLORIS) instrument on the FLEX satellite is planned to come with two main improvements: a finer spatial resolution and a higher signal-to-noise ratio. Additionally, FLEX data will be evaluated with the help of ground-based calibration-validation dataset, which is expected to help the interpretation of the FLEX data, providing an absolute ϕ_F scale. The spatial footprint of FLEX is in the same order of magnitude as the footprint of eddy covariance towers, allowing for a fairer comparison of spaceborne ϕ_F and eddy covariance estimates of Gs. A better characterization of this link will help to improve global estimates of photosynthesis and transpiration. However, the main advantage of the TROPOSIF product compared to the upcoming FLEX data is the higher temporal resolution of TROPOMI. A synergetic interpretation of both datasets might allow for ϕ_F and Gs estimations that are both accurate and frequent.

4.6. Perspectives for upcoming geostationary missions

In addition to the FLEX mission, the recently launched Tropospheric Emissions: Monitoring of POllution (TEMPO) mission, as well as the upcoming Sentinel-4 sensor on the Meteosat Third Generation-Sounder (MTG-S) satellite, will have capabilities of measuring SIF data (Jonard et al., 2020). Unlike to the TROPOMI or the FLEX mission, these missions are in geostationary orbit, allowing them to capture the diurnal dynamics in fluorescence emission. This opens the door for detecting the afternoon depression, a decrease in photosynthesis (Xiao et al., 2021). Thermal-based geostationary data have already made use of the afternoon depression to reveal drought stress during the 2020 US Heatwave (Li et al., 2023).

5. Conclusion

While well-established in laboratory experiments, the fluorescence yield (ϕ_F) retrieved from remote sensing platforms is a newly established variable. Mechanistically linked to the photosynthetic electron transport, ϕ_F is promising for large-scale monitoring of vegetation water status and functioning. Here, ϕ_F has been retrieved at the global scale by normalizing the TROPOMI SIF data with the NIRvP, the latter accounting for the irradiation and canopy structure components of the signal. To gain insight into the environmental controls on the remotely sensed ϕ_F, the global ϕ_F data were set out in a phase space with remotely sensed vapour pressure deficit (VPD) and soil moisture (SM), from the AIRS and SMAP sensors, respectively. The global spatial patterns of ϕ_F show that these are responsive to limiting factors of photosynthesis, including water availability, solar irradiation or temperature, among others. Water availability and demand is described by the SM and VPD and drive ϕ_F variability in both the spatial and temporal domains. Consequently, ϕ_F shows a maximum around intermediate soil moisture and VPD (i.e., 0.1 $m^3/m^3 < SM < 0.3 \; m^3/m^3$ and 1.5 kPa<VPD<2.5 kPa). Results show that lower SM and/or higher VPD may lead to lowered stomatal conductance. The effect of high VPD and low SM on ϕ_F is stronger for more isohydric ecosystems, as they exert stricter control over their stomatal conductance and thus also over their photosynthetic electron transport and water regulation in function of the environmental variables. More anisohydric ecosystems tend to have less strict control on their stomatal closure, allowing to maintain high rates of photosynthesis and therefore experience a weaker control of SM and VPD on ϕ_F. The ecosystem-level link between Gs and ϕ_F obtained through remote sensing data is consistent with the link between these variables at the leaf scale. At the leaf scale, the increase in NPQ is an essential factor for linking Gs and ϕ_F. Despite of NPQ not being measurable from a remote sensing platform, it makes sense to believe that the NPQ is equally important to link ϕ_F and Gs at the global scale.

Thanks to its sensitivity to VPD and SM, and carrying an imprint from Gs, ϕ_F is a very promising emerging remote sensing signal that is sensitive to the photosynthetic electron transport at the instant of the measurement. Still, we note that neither ϕ_F nor Gs datasets have been validated with site (e.g., airborne, eddy-covariance towers, etc.) data, so further comparison and validation of these datasets should be done in the future. In the case of SIF and the reflectance bands used in ϕ_F calculation, some calibration and validation activities will be undertaken for the FLEX mission. The instantaneous nature of the stress information embedded in ϕ_F contrasts with traditional, greenness-based indicators that reflect a stress legacy effect than the instantaneous stress itself. The FLEX satellite, scheduled for launch in 2025 will retrieve ϕ_F at a finer spatial scale, a finer spectral resolution, and a higher signal-to-noise ratio. This opens the door for field-scale analyses and satellite-based modelling with ϕ_F.

Acknowledgements

This research was funded by the Fonds pour la Formation à la Recherche dans l'Industrie et dans l'Agriculture (FRIA, Belgium). We would like to thank Andrea Carminati, Fabian Wankmüller and Peter Lehmann, all from ETH Zurich, for their help and support regarding the soil-plant hydraulic model.

References

Acebron, K., Matsubara, S., Jedmowski, C., Emin, D., Muller, O., Rascher, U., 2021. Diurnal dynamics of nonphotochemical quenching in Arabidopsis npq mutants assessed by solar-induced fluorescence and reflectance measurements in the field. New Phytologist 229, 2104–2119. doi:`10.1111/nph.16984`.

Alonso, L., Van Wittenberghe, S., Amorós-López, J., Vila-Francés, J., Gómez-Chova, L., Moreno, J., 2017. Diurnal cycle relationships between passive fluorescence, PRI and NPQ of vegetation in a controlled stress experiment. Remote Sensing 9. doi:`10.3390/rs9080770`.

Attia, Z., Domec, J.C., Oren, R., Way, D.A., Moshelion, M., 2015. Growth and physiological responses of isohydric and anisohydric poplars to drought. Journal of Experimental Botany 66, 4373–4381. doi:`10.1093/jxb/erv195`.

Aumann, H.H., Chahine, M.T., Gautier, C., Goldberg, M.D., Kalnay, E., McMillin, L.M., Revercomb, H., Rosenkranz, P.W., Smith, W.L., Staelin, D.H., Strow, L.L., Susskind, J., 2003. AIRS/AMSU/HSB on the aqua mission: Design, science objectives, data products, and processing systems. IEEE Transactions on Geoscience and Remote Sensing 41, 253–263. doi:`10.1109/TGRS.2002.808356`.

Balting, D.F., AghaKouchak, A., Lohmann, G., Ionita, M., 2021. Northern Hemisphere drought risk in a warming climate. npj Climate and Atmospheric Science 4, 1–13. doi:`10.1038/s41612-021-00218-2`.

Bauer, H., Ache, P., Lautner, S., Fromm, J., Hartung, W., Al-Rasheid, K.A., Sonnewald, S., Sonnewald, U., Kneitz, S., Lachmann, N., Mendel, R.R., Bittner, F., Hetherington, A.M., Hedrich, R., 2013. The stomatal response to reduced relative humidity requires guard cell-autonomous ABA synthesis. Current Biology 23, 53–57. doi:`10.1016/j.cub.2012.11.022`.

Bayat, B., Van Der Tol, C., Verhoef, W., 2018. Integrating satellite optical and thermal infrared observations for improving daily ecosystem functioning estimations during a drought episode. Remote Sensing of Environment 209, 375–394. doi:`10.1109/IGARSS.2018.8518309`.

Berger, K., Machwitz, M., Kycko, M., Kefauver, S., Van Wittenberghe, S., Gerhards, M., Verrelst, J., Atzberger, C., van der Tol, C., Damm, A., Rascher, U., Herrmann, I., Sobejano Paz, V., Fahrner, S., Pieruschka, R., Prikaziuk, E., Buchaillot, L., Halabuk, A., Celesti, M., Koren, G., Gormus, E., Rossini, M., Foerster, M., Siegmann, B., Abdelbaki, A., Tagliabue, G., Hank, T., Darvischzadeh, R., Aasen, H., Garcia, M., Pocas, I., Bandopadhyay, S., Sulis, M., Tomelleri, E., Rozenstein, O., Filchev, L., Stancile, G., Schlerf, M., 2022. Multi-sensor spectral synergies for crop stress detection and monitoring in the optical domain: a review. Remote Sensing of Environment 280.

Blauhut, V., Stoelzle, M., Ahopelto, L., Brunner, M.I., Teutschbein, C., Wendt, D.E., Akstinas, V., Bakke, S.J., Barker, L.J., Bartošová, L., Briede, A., Cammalleri, C., Kalin, K.C., De Stefano, L., Fendeková, M., Finger, D.C., Huysmans, M., Ivanov, M., Jaagus, J., Jakubínský, J., Krakovska, S., Laaha, G., Lakatos, M., Manevski, K., Neumann Andersen, M., Nikolova, N., Osuch, M., Van Oel, P., Radeva, K., Romanowicz, R.J., Toth, E., Trnka, M., Urošev, M., Urquijo Reguera, J., Sauquet, E., Stevkov, A., Tallaksen, L.M., Trofimova, I., Van Loon, A.F., Van Vliet, M.T., Vidal, J.P., Wanders, N., Werner, M., Willems, P., Zivković, N., 2022. Lessons from the 2018-2019 European droughts: a collective need for unifying drought risk management. Natural Hazards and Earth System Sciences 22, 2201–2217. doi:`10.5194/nhess-22-2201-2022`.

Bussotti, F., Gerosa, G., Digrado, A., Pollastrini, M., 2020. Selection of chlorophyll fluorescence parameters as indicators of photosynthetic efficiency in large scale plant ecological studies 108.

Cao, J., An, Q., Zhang, X., Xu, S., Si, T., Niyogi, D., 2021. Is satellite Sun-Induced Chlorophyll Fluorescence more indicative than vegetation indices under drought condition? Science of the Total Environment 792. doi:`10.1016/j.scitotenv.2021.148396`.

Carminati, A., Javaux, M., 2020. Soil Rather Than Xylem Vulnerability Controls Stomatal Response to Drought. Trends in Plant Science 25, 868–880. doi:`10.1016/j.tplants.2020.04.003`.

Cocozza, C., De Miguel, M., Pšidová, E., Ditmarová, L., Marino, S., Maiuro, L., Alvino, A., Czajkowski, T., Bolte, A., Tognetti, R., 2016. Variation in ecophysiological traits and drought tolerance of beech (Fagus sylvatica L.) seedlings from different populations. Frontiers in Plant Science 7, 1–14. doi:`10.3389/fpls.2016.00886`.

De Cannière, S., Herbst, M., Vereecken, H., Defourny, P., Jonard, F., 2021.

Constraining water limitation of photosynthesis in a crop growth model with sun-induced chlorophyll fluorescence. Remote Sensing of Environment 267. doi:`10.1016/j.rse.2021.112722`.

De Canniere, S., Vereecken, H., Defourny, P., Jonard, F., 2022. Remote Sensing of Instantaneous Drought Stress at Canopy Level Using Sun-Induced Chlorophyll Fluorescence and Canopy Reflectance. Remote Sensing 14.

Dechant, B., Ryu, Y., Badgley, G., Köhler, P., Rascher, U., Migliavacca, M., Zhang, Y., Tagliabue, G., Guan, K., Rossini, M., Goulas, Y., Zeng, Y., Frankenberg, C., Berry, J.A., 2022. NIRVP: A robust structural proxy for sun-induced chlorophyll fluorescence and photosynthesis across scales. Remote Sensing of Environment 268. doi:`10.1016/j.rse.2021.112763`.

Dechant, B., Ryu, Y., Badgley, G., Zeng, Y., Berry, J.A., Zhang, Y., Goulas, Y., Li, Z., Zhang, Q., Kang, M., Li, J., Moya, I., 2020. Canopy structure explains the relationship between photosynthesis and sun-induced chlorophyll fluorescence in crops. Remote Sensing of Environment 241. doi:`10.1016/j.rse.2020.111733`.

Didan, K., 2015. MOD13C1 MODIS/Terra Vegetation Indices 16-Day L3 Global 0.05Deg CMG V006No Title. doi:`https://doi.org/10.5067/MODIS/MOD13C1.006`.

Drusch, M., Moreno, J., Bello, U.D., Franco, R., Goulas, Y., Huth, A., Kraft, S., Middleton, E.M., Miglietta, F., Mohammed, G., Nedbal, L., Rascher, U., Schüttemeyer, D., Verhoef, W., 2017. Concept — ESA ' s Earth Explorer 8. IEEE Trans. Geosci. Remote Sens. 55, 1273–1284.

Entekhabi, B.D., Njoku, E.G., Neill, P.E.O., Kellogg, K.H., Crow, W.T., Edelstein, W.N., Entin, J.K., Goodman, S.D., Jackson, T.J., Johnson, J., Kimball, J., Piepmeier, J.R., Koster, R.D., Martin, N., Mcdonald, K.C., Moghaddam, M., Moran, S., Reichle, R., Shi, J.C., Spencer, M.W., Thurman, S.W., Tsang, L., Zyl, J.V., 2010. The SoilMoistureActive Passive (SMAP) Mission 98.

Farquhar, G., von Caemmerer, S., Berry, J., 1980. A biochemical-model of photosynthetic CO2 assimilation in leaves of C3 species. Planta 149, 78–90.

Feldman, A., Konings, A., Piles, M., Entekhabi, D., 2021. The multi-temporal dual channel algorithm (mt-dca). doi:`10.5281/zenodo.5619583`.

Feldman, A.F., Short Gianotti, D.J., Trigo, I.F., Salvucci, G.D., Entekhabi, D., 2020. Land-Atmosphere Drivers of Landscape-Scale Plant Water Content Loss. Geophysical Research Letters 47. doi:`10.1029/2020GL090331`.

Flexas, J., Escalona, J.M., Evain, S., Gulías, J., Moya, I., Osmond, C.B., Medrano, H., 2002. Steady-state chlorophyll fluorescence (Fs) measurements as a tool to follow variations of net CO2 assimilation and stomatal conductance during water-stress in C3 plants. Physiologia Plantarum , 26–29.

Friedl, M.A., Sulla-Menashe, D., Tan, B., Schneider, A., Ramankutty, N., Sibley, A., Huang, X., 2010. MODIS Collection 5 global land cover: Algorithm refinements and characterization of new datasets. Remote Sensing of Environment 114, 168–182. doi:`10.1016/j.rse.2009.08.016`.

Fu, Z., Ciais, P., Prentice, I.C., Bastos, A., Luo, X., Green, J.K., Gentine, P., Makowski, D., Stoy, P.C., Yang, H., Hajima, T., 2022. Along a Large Range of Soil Water De Fi Cits. Nature Communiacations 13, 989–999.

Fujimura, S., Shi, P., Iwama, K., Zhang, X., Gopal, J., Jitsuyama, Y., 2010. Effect of altitude on the response of net photosynthetic rate to carbon dioxide increase by spring wheat. Plant Production Science 13, 141–149. doi:`10.1626/pps.13.141`.

Gong, F., Chen, X., Yuan, W., Su, Y., Yang, X., Liu, L., Sun, Q., Wu, J., Dai, Y., Shang, J., 2022. Partitioning of three phenology rhythms in American tropical and subtropical forests using remotely sensed solar-induced chlorophyll fluorescence and field litterfall observations. International Journal of Applied Earth Observation and Geoinformation 107, 102698. doi:`10.1016/j.jag.2022.102698`.

Gu, H., Yin, G., Yang, Y., Verger, A., Filella, I., Zeng, Y., Hao, D., Xie, Q., Li, X., Xiao, J., 2023. Satellite-detected Contrasting Responses of Canopy Structure and Leaf Physiology to Drought. Journal of Selected Topics in Applied Earth Observation and Remote Sensing , 1–10doi:`10.1109/JSTARS.2023.3247422`.

Guanter, L., Bacour, C., Schneider, A., Aben, I., Van Kempen, T.A., Maignan, F., Retscher, C., Köhler, P., Frankenberg, C., Joiner, J., Zhang, Y., 2021. The TROPOSIF global sun-induced fluorescence dataset from the Sentinel-5P TROPOMI mission. Earth System Science Data 13, 5423–5440. doi:`10.5194/essd-13-5423-2021`.

Guanter, L., Zhang, Y., Jung, M., Joiner, J., Voigt, M., Berry, J.A., Frankenberg, C., Huete, A.R., Zarco-Tejada, P., Lee, J.E., Moran, M.S., Ponce-Campos, G., Beer, C., Camps-Valls, G., Buchmann, N., Gianelle, D., Klumpp, K., Cescatti, A., Baker, J.M., Griffis, T.J., 2014. Global and time-resolved monitoring of crop photosynthesis with chlorophyll fluorescence. Proceedings of the National Academy of Sciences of the United States of America 111. doi:`10.1073/pnas.1320008111`.

Gupta, A., Rico-Medina, A., Caño-Delgado, A.I., 2020. The physiology of plant responses to drought. Science 368, 266–269. doi:`10.1126/science.aaz7614`.

He, L., Wood, J.D., Sun, Y., Magney, T., Dutta, D., Köhler, P., Zhang, Y., Yin, Y., Frankenberg, C., 2020. Tracking Seasonal and Interannual Variability in Photosynthetic Downregulation in Response to Water Stress at a Temperate Deciduous Forest. Journal of Geophysical Research: Biogeosciences 125, 1–23. doi:`10.1029/2018JG005002`.

Helm, L., Shi, H., Lerdau, M., Yang, X., 2020. Solar-induced chlorophyll fl uorescence and short-term photosynthetic response to drought. Ecological applications 30, 1–12.

Hengl, T., 2018a. Clay content in % (kg / kg) at 6 standard depths (0, 10, 30, 60, 100 and 200 cm) at 250 m resolution. doi:`10.5281/zenodo.2525663`.

Hengl, T., 2018b. Sand content in % (kg / kg) at 6 standard depths (0, 10, 30, 60, 100 and 200 cm) at 250 m resolution. doi:`10.5281/zenodo.2525662`.

Jonard, F., Andre, F., Ponette, Q., Vincke, C., Jonard, M., 2011. Sap flux density and stomatal conductance of European beech and common oak trees in pure and mixed stands during the summer drought of 2003. Journal of Hydrology 409, 371–381. doi:`10.1016/j.jhydrol.2011.08.032`.

Jonard, F., De Cannière, S., Brüggemann, N., Gentine, P., Short Gianotti, D.J., Lobet, G., Miralles, D.G., Montzka, C., Pagán, B.R., Rascher, U., Vereecken, H., 2020. Value of sun-induced chlorophyll fluorescence for quantifying hydrological states and fluxes: Current status and challenges. Agricultural and Forest Meteorology 291.

Jonard, F., Feldman, A.F., Short Gianotti, D.J., Entekhabi, D., 2022. Observed water and light limitation across global ecosystems. Biogeosciences 19, 5575–5590. doi:`10.5194/bg-19-5575-2022`.

Kimm, H., Guan, K., Burroughs, C.H., Peng, B., Ainsworth, E.A., Bernacchi, C.J., Moore, C.E., Kumagai, E., Yang, X., Berry, J.A., Wu, G., 2021a. Quantifying high-temperature stress on soybean canopy photosynthesis: The unique role of sun-induced chlorophyll fluorescence. Global Change Biology 27, 2403–2415. doi:`10.1111/gcb.15603`.

Kimm, H., Guan, K., Jiang, C., Miao, G., Wu, G., Suyker, A.E., Ainsworth, E.A., Bernacchi, C.J., Montes, C.M., Berry, J.A., Yang, X., Frankenberg, C., Chen, M., Köhler, P., 2021b. A physiological signal derived from sun-induced chlorophyll fluorescence quantifies crop physiological response to environmental stresses in the U.S. Corn Belt. Environmental Research Letters 16. doi:`10.1088/1748-9326/ac3b16`.

Konings, A.G., Gentine, P., 2017. Global variations in ecosystem-scale isohydricity. Global Change Biology 23, 891–905. doi:`10.1111/gcb.13389`.

Konings, A.G., Piles, M., Das, N.N., Entekhabi, D., 2017. L-band vegetation optical depth and effective scattering albedo estimation from SMAP. Remote Sensing of Environment 198, 460–470.

Lee, J.E., Berry, J.A., van der Tol, C., Yang, X., Guanter, L., Damm, A., Baker, I., Frankenberg, C., 2015. Simulations of chlorophyll fluorescence incorporated into the Community Land Model version 4. Global Change Biology 21, 3469–3477.

Li, X., Ryu, Y., Xiao, J., Dechant, B., Liu, J., Li, B., Jeong, S., Gentine, P., 2023. New-generation geostationary satellite reveals widespread midday depression in dryland photosynthesis during 2020 western U.S. heatwave. Science Advances 9, 1–15. doi:`10.1126/sciadv.adi0775`.

Liu, L., Gudmundsson, L., Hauser, M., Qin, D., Shuangcheng, L., Seneviratne, S., 2020. Soil moisture dominates dryness stress on ecosystem production globally. Nature Communications 11. doi:`10.1038/s41467-020-18631-1`.

Lu, H., Qin, Z., Lin, S., Chen, X., Chen, B., He, B., Wei, J., Yuan, W., 2022. Large influence of atmospheric vapor pressure deficit on ecosystem production efficiency. Nature Communications 13, 10–13. doi:`10.1038/s41467-022-29009-w`.

Maes, W., Steppe, K., 2012. Estimating evapotranspiration with ground-based thermal remote sensing in agriculture: a review. Journal of Experimental Botany 63, 695–709. doi:`10.1093/jxb/err313`.

Medlyn, B., Duursma, R., Eamus, D., Ellsworth, D., Prentice, C., Bartons, C., Crous, K., De Angelis, P., Freeman, M., Wingate, L., 2011. Reconciling the optimal and empirical approaches to modelling stomatal conductance. Global Change Biology 2, 2134–2144. doi:`10.1111/j.1365-2486.2010.02375.x`.

Muhammad, I., Shalmani, A., Ali, M., Yang, Q.H., Ahmad, H., Li, F.B., 2021. Mechanisms Regulating the Dynamics of Photosynthesis Under Abiotic Stresses. Frontiers in Plant Science 11, 1–25. doi:`10.3389/fpls.2020.615942`.

Novick, K.A., Ficklin, D.L., Stoy, P.C., Williams, C.A., Bohrer, G., Oishi, A.C., Papuga, S.A., Blanken, P.D., Noormets, A., Sulman, B.N., Scott, R.L., Wang, L., Phillips, R.P., 2016. The increasing importance of atmospheric demand for ecosystem water and carbon fluxes. Nature Climate Change 6, 1023–1027. doi:`10.1038/nclimate3114`.

Novick, K.A., Konings, A.G., Gentine, P., 2019. Beyond soil water potential: An expanded view on isohydricity including land–atmosphere interactions and phenology. Plant Cell and Environment 42, 1802–1815. doi:`10.1111/pce.13517`.

O, S., Hou, X., Orth, R., 2020. Observational evidence of wildfire-promoting soil moisture anomalies. Scientific Reports 10, 11008. doi:`10.1038/s41598-020-67530-4`.

Orimoloye, I.R., 2022. Agricultural Drought and Its Potential Impacts: Enabling Decision-Support for Food Security in Vulnerable Regions. Frontiers in Sustainable Food Systems 6. doi:`10.3389/fsufs.2022.838824`.

Pinto, F., Damm, A., Schickling, A., Panigada, C., Cogliati, S., Müller-linow, M., Ballvora, A., 2016. Sun-induced chlorophyll fluorescence from high-resolution imaging spectroscopy data to quantify spatio-temporal patterns of photosynthetic function in crop canopies. Plant Cell and Environment 39, 1500–1512. doi:`10.1111/pce.12710`.

Porcar-Castell, A., Malenovský, Z., Magney, T., Wittenberghe, S.V., Fernández-marín, B., Maignan, F., Zhang, Y., Maseyk, K., Atherton, J., Albert, L.P., Robson, T.M., Zhao, F., Ensminger, I., Rajewicz, P.A., Grebe, S., 2021. Chlorophyll a fluorescence illuminates a path connecting plant molecular biology to Earth-system science. Nature plants 7.

Porcar-Castell, A., Tyystjärvi, E., Atherton, J., van der Tol, C., Flexas, J., Pfündel, E.E., Moreno, J., Frankenberg, C., Berry, J.A., 2014. Linking chlorophyll a fluorescence to photosynthesis for remote sensing applications: mechanisms and challenges. Journal of Experimental Botany 65, 4065–4095.

Qiu, B., Xue, Y., Fisher, J.B., Guo, W., Berry, J.A., Zhang, Y., 2018. Satellite Chlorophyll Fluorescence and Soil Moisture Observations Lead to Advances in the Predictive Understanding of Global Terrestrial Coupled Carbon-Water Cycles. Global Biogeochemical Cycles 32, 360–375.

Qiu, R., Li, X., Han, G., Xiao, J., Ma, X., Gong, W., 2022. Monitoring drought impacts on crop productivity of the U.S. Midwest with solar-induced fluorescence: GOSIF outperforms GOME-2 SIF and MODIS NDVI, EVI, and NIRv. Agricultural and Forest Meteorology 323, 109038. doi:`10.1016/j.agrformet.2022.109038`.

Rawls, W.J., Brakensiek, D.L., 1985. Prediction of soil water properties for hydrologic modeling, in: Watershed management in the eighties, ASCE. pp. 293–299.

Ryu, Y., Berry, J.A., Baldocchi, D.D., 2019. Remote Sensing of Environment What is global photosynthesis ? History , uncertainties and opportunities 223, 95–114.

Sulman, B.N., Roman, D.T., Yi, K., Wang, L., Phillips, R.P., Novick, K.A., 2016. High atmospheric demand for water can limit forest carbon uptake and transpiration as severely as dry soil. Geophysical Research Letters 43, 9686–9695. doi:`10.1002/2016GL069416`.

Sun, Y., Fu, R., Dikinson, R., Joiner, J., Frankenberg, C., Gu, L., Xia, Y., Fernando, N., 2015. Drought onset mechanisms revealed by satellite solar-induced chlorophyll fluorescence: Insights from two contrasting extreme events. Journal of Geophysical Research: Biogeosciences 120, 707–723. doi:`10.1002/2015JG003150.Received`.

Svadoba, M., LeCompte, D., Hayes, M., Heim, R., Gleason, K., Angel, J., Rippey, B., Tinker, R., Palecki, M., Stooksbury, D., Miskus, D., Stephens, S., 2002. The drought monitor. Bulletins of the American Meteorological Sociecty , 1181–1190.

Tagesson, T., Fensholt, R., Guiro, I., Rasmussen, M.O., Huber, S., Mbow, C., Garcia, M., Horion, S., Sandholt, I., Holm-Rasmussen, B., Göttsche, F.M., Ridler, M.E., Olén, N., Lundegard Olsen, J., Ehammer, A., Madsen, M., Olesen, F.S., Ardö, J., 2015. Ecosystem properties of semiarid savanna grassland in West Africa and its relationship with environmental variability. Global Change Biology 21, 250–264. doi:`10.1111/gcb.12734`.

van der Tol, C., Berry, J.A., Campbell, P.K., Rascher, U., 2014. Models of fluorescence and photosynthesis for interpreting measurements of solar-induced chlorophyll fluorescence. Journal of Geophysical Research: Biogeosciences 119, 2312–2327. doi:`10.1002/2014JG002713`.

Venturas, M.D., Todd, H.N., Trugman, A.T., Anderegg, W.R.L., 2021. Understanding and predicting forest mortality in the western United States using long-term forest inventory data and modeled hydraulic damage. New Phytologist 230, 1896–1910. doi:`10.1111/nph.17043`.

Wang, N., Yang, P., Clevers, J.G.P.W., Wieneke, S., Kooistra, L., 2023. Decoupling physiological and non-physiological responses of sugar beet to water stress from sun-induced chlorophyll fluorescence Remote Sensing of Environment Decoupling physiological and non-physiological responses of sugar beet to water stress from sun-. Remote Sensing of Environment 286, 113445. doi:`10.1016/j.rse.2022.113445`.

Wankmüller, F.J.P., Carminati, A., 2021. Stomatal regulation prevents plants from critical water potentials during drought: Result of a model linking soil–plant hydraulics to abscisic acid dynamics. Ecohydrology , 1–15doi:`10.1002/eco.2386`.

West, H., Quinn, N., Horswell, M., 2019. Remote sensing for drought monitoring and impact assessment: Progress, past challenges and future opportunities. Remote Sensing of Environment 232, 111291. doi:`10.1016/j.rse.2019.111291`.

West, H., Quinn, N., Horswell, M., White, P., 2018. Assessing vegetation response to soil moisture fluctuation under extreme drought using sentinel-2. Water (Switzerland) 10, 1–22. doi:`10.3390/w10070838`.

Wieneke, S., Ahrends, H., Damm, A., Pinto, F., Stadler, A., Rossini, M., Rascher, U., 2016. Remote Sensing of Environment Airborne based spectroscopy of red and far-red sun-induced chlorophyll fl uorescence : Implications for improved estimates of gross primary productivity. Remote Sensing of Environment 184, 654–667. doi:`10.1016/j.rse.2016.07.025`.

Wong, C.Y.S., Young, D.J.N., Latimer, A.M., Buckley, T.N., Magney, T.S., 2021. Remote Sensing of Environment Importance of the legacy effect for assessing spatiotemporal correspondence between interannual tree-ring width and remote sensing products in the Sierra Nevada. Remote Sensing of Environment 265, 112635. doi:`10.1016/j.rse.2021.112635`.

Wu, G., Guan, K., Li, Y., Novick, K.A., Feng, X., McDowell, N.G., Konings, A.G., Thompson, S.E., Kimball, J.S., De Kauwe, M.G., Ainsworth, E.A., Jiang, C., 2021. Interannual variability of ecosystem iso/anisohydry is regulated by environmental dryness. New Phytologist 229, 2562–2575. doi:`10.1111/nph.17040`.

Wu, G., Guan, K., Li, Y., Novick, K.A., Konings, A.G., Thompson, S.E., Kimball, J.S., Kauwe, M.G.D., 2020. Interannual variability of ecosystem iso / anisohydry is regulated by environmental dryness doi:`10.1111/nph.17040`.

Xiao, J., Fisher, J.B., Hashimoto, H., Ichii, K., Parazoo, N.C., 2021. Emerging satellite observations for diurnal cycling of ecosystem processes. Nature Plants 7, 877–887. URL: `http://dx.doi.org/10.1038/s41477-021-00952-8`, doi:`10.1038/s41477-021-00952-8`.

Xu, S., Atherton, J., Riikonen, A., Zhang, C., Oivukkamäki, J., MacArthur, A., Honkavaara, E., Hakala, T., Koivumäki, N., Liu, Z., Porcar-Castell, A., 2021. Structural and photosynthetic dynamics mediate the response of SIF to water stress in a potato crop. Remote Sensing of Environment 263. doi:`10.1016/j.rse.2021.112555`.

Yang, P., 2022. Exploring the interrelated effects of soil background, canopy structure and sun-observer geometry on canopy photochemical reflectance index. Remote Sensing of Environment 279. doi:`10.1016/j.rse.2022.113133`.

Yang, P., van der Tol, C., 2018. Linking canopy scattering of far-red sun-induced chlorophyll fluorescence with reflectance. Remote Sensing of Environment 209, 456–467.

Zarco-Tejada, P.J., Gonzalez-Dugo, V., Berni, J.A., 2012. Fluorescence, temperature and narrow-band indices acquired from a UAV platform for water stress detection using a micro-hyperspectral imager and a thermal camera.

Remote Sensing of Environment 117, 322–337. doi:`10.1016/j.rse.2011.10.007`.

Zeng, Y., Chen, M., Hao, D., Damm, A., Badgley, G., Rascher, U., Johnson, J.E., Dechant, B., Siegmann, B., Ryu, Y., Qiu, H., Krieger, V., Panigada, C., Celesti, M., Miglietta, F., Yang, X., Berry, J.A., 2022. Combining near-infrared radiance of vegetation and fluorescence spectroscopy to detect effects of abiotic changes and stresses. Remote Sensing of Environment 270.

Zhang, J., Guan, K., Peng, B., Pan, M., Zhou, W., Jiang, C., Kimm, H., Franz, T.E., Grant, R.F., Yang, Y., Rudnick, D.R., Heeren, D.M., Suyker, A.E., Bauerle, W.L., Miner, G.L., 2021. Sustainable irrigation based on co-regulation of soil water supply and atmospheric evaporative demand. Nature Communications 12. doi:`10.1038/s41467-021-25254-7`.

Zhang, Y., Fang, J., Smith, W., Wang, X., Gentine, P., Scott, R., Migliavacca, M., Jeong, S., Litvak, M., Zhou, S., 2023. Satellite solar-induced chlorophyll fluorescence tracks physiological development during 2020 southwest US drought drought stress Running. Global Change Biology , 1–15doi:`10.1111/gcb.16683`.

Appendix A. Supplementary figures